2015

Design of High-Efficiency Rare-Earth Permanent Magnet Synchronous Motor and Drive System

Hanzhou Liu
University of Central Florida

DESIGN OF HIGH-EFFICIENCY RARE-EARTH PERMANENT MAGNET SYNCHRONOUS MOTOR AND DRIVE SYSTEM

by

HANZHOU LIU
M.S. in Electrical Engineering, University of Central Florida, 2010

A dissertation submitted in partial fulfilment of the requirements
for the degree of Doctor of Philosophy
in the Department of Electrical Engineering and Computer Science
in the College of Engineering and Computer Science
at the University of Central Florida
Orlando, Florida

Summer Term
2015

Major Advisor: Thomas Wu

ABSTRACT

Utilization of renewable energy has become the future trend in the trucking industry. Electrical power generated from renewable energy can replace part of the fuel usage. There is usually limited space for storing on-board battery. Thus, to better utilize the battery power, it becomes critical to have an efficient energy conversion device that can transfer energy from battery to amenities such as air conditioner, microwave, TV, mini refrigerator, etc. In this dissertation, a designed permanent magnet synchronous motor (PMSM) can be such energy conversion device for an electric Auxiliary Power Unit (APU) application, which will have a desired output power of 2 kW at 2 krpm, and maintain an efficiency greater than 90%. The design calls for good performance over a speed range of 1.5 krpm to 2.5 krpm. The current air conditioning system for automobile works only by "on" or "off" mode. For the heat mode, that means it is on with heat once the cabin temperature drops down to a level and off if the temperature rises back above that level. For the cool mode, that means it is on with cold air once the cabin temperature rises above a level, and off if the temperature drops back to that level. This is because the motor does not have the speed control functionality according to the temperature variation and people in the cabin do not feel much comfortable for that temperature change periodically as well as the inefficient energy consumption. With our novel technology, the designed motor can adjust its speed through the embedded system of our novel DC to AC inverter to provide a variable load. For example, with high efficiency, the fully charged battery sets (48 volts) can supply the electrical power and cooling to the cabin for about 10 hours without recharging using the main engine.

Copper loss is the most significant part of all the losses in low speed electric machines. Reducing the copper loss is the key to build highly efficient machine. We use copper wires with the current density lower than traditional design which result in large cross section of the wire and thus reduce the copper loss and improve the efficiency. This also makes thermal management easier and reduces the need to use active cooling methodologies (such as fan, liquid cooling or spray

cooling); and hence the overall power density of the whole system (including cooling devices) will not decease much. In traditional machine design, the torque angle is designed to be in the range of 15 to 30 degrees at the rated power and speed. In our high efficiency motor design, we propose to use much lower torque angle of 2 to 15 degrees at the rated power and speed. Such design can effectively increase the overload power handling capability and efficiency. Besides, small torque angle will result in large airgap size and increased thickness of the permanent magnets. Large airgap helps to reduce the windage loss of the machine and generates a lot less mechanical noise based on our design experience. Increased thickness of the permanent magnets helps to avoid the demagnetization.

As the technology of advanced micro-controller develops, fast-response power electronic devices can be used in the motor controller. A novel design of DC to AC inverter with the field oriented control scheme and sliding mode observer algorithm for driving the designed motor is developed. The inverter has the capability of driving the motor with its output power at 2 kW.

To my family,

for their love and sacrifices.

ACKNOWLEDGMENTS

This dissertation includes many years of research, hard work and experiences. I have benefited tremendously from the guidance of many other researchers.

I would like to thank a lot of people who have contributed to this work. Firstly, I am indebted to my major advisor, Dr. Thomas Wu, for his precious guidance, support, and encouragement. The knowledge that I have learned from him will benefit me throughout the years.

My Ph.D career was made memorable in a large part due to my lab mates at University of Central Florida. I would like to thank Dr. Zhigang Gao for his guidance on my research topic. I would like to thank Eric Lin, David Woodburn, Kejiu Zhang and other fellows for sharing their valuable experience with me during my many years of journey. I especially thank David for his guidance which made me gone through those difficulties.

I would like to take this opportunity to thank Dr. Louis Chow and Dr. Wei Wu for their help on my research. I also would like to thank all of my other committee members: Dr. Issa Batarseh, Dr. Michael Haralambous and Dr. Mingjie Lin for their comments on my research.

I should thank Ying, Yalin, Liyue, Yang and many other friends for traveling the journey together with me. It is their accompany that made my life in Orlando unforgettable.

I owe everything to my grandparents, parents, and other family members. It is through their selfless dedication and sacrifices that I have come this far.

TABLE OF CONTENTS

LIST OF FIGURES

LIST OF TABLES

CHAPTER 1: INTRODUCTION

A lot of applications have electric motor at their heart. For example, washing machines, CD players, vacuum robot, hair dyers, electric tooth brush, etc. The list would be endless; most of the electric appliances have either simple or complex electric motor inside them. Since the first real rotating electric motor was created in 1834, a lot of other researchers in the world started to build similar motors and later with better and better improved performance. DC motor was originally developed from the power generators. It includes the brush commutator. DC motor is used especially in the applications of low power and low voltage ranges [1] - [3]. In the late 19th century, people invented the three-phase electric power system, which is the basis for modern electrical power system and more advanced electric machines. Around the same time, three-phase induction motor and three-phase synchronous motor were invented which become the most popular machines in the industry [4] - [12]. Currently, there are motor applications everywhere in our daily life.

Synchronous machine means that the magnetic field generated by the stator windings rotates with the same speed as the rotor; or asynchronous, means that there is a speed difference. Induction machine is defined in a way when rotor winding is powered, from which it generates a magnetic field, interacting with the stator magnetic field. People normally categorize induction machines as asynchronous machines. They have been widely used because of the simplicity and low cost. They dominate the market in applications which efficiency is not a high priority factor. Obviously, the advantage of the induction machine over brush machine is no brush further required since it is a consuming component that have to be replaced periodically which increases the maintenance burden [13] - [14].

Synchronous machines can achieve higher efficiency than induction machines. However, due to the cost and design complexity they are not as widely used as induction machines. AC reluctance machines have saliency on the rotor so that the windings powered on stator can exert

torque on the rotor. Windings on the stator are grouped into several sub-groups. By controlling the direction of the current flowing through individual sub-groups, it is possible to generate the torque with the same direction which moves the rotor [15] - [22].

Permanent magnet machines have become the most advanced machines. Research on that is a very popular topic. The big difference between the PM machines and the induction machines is that the rotor windings are replaced by the permanent magnets which leads to high efficiency due to the absence of the copper wires. It is usually driven by a three-phase balanced sinusoidal voltage source as the electromagnet (EM). Since it does not require excitation and commutation circuit, the maintenance required for the excitation circuit and the copper loss on the rotor are both effectively eliminated. The efficiency can be improved by 2 - 8% compared to the induction motor of the same power rating. The PMSM can maintain a high efficiency when its output power varies from 50 - 120% of the rated power. In addition, PMSM has many other advantages: it is reliable even at super high speed; advanced sensorless control method is possible; the output torque ripple is very small, etc. [23] - [36]. The future direction of the PMSM research is to make the machine to be more compact and have higher power density, higher torque, higher rotating speed and lighter weight.

Researchers try to develop new methods to minimize the power losses in order to boost up the efficiency of the motor. With a better structure of PMSM, people are hopeful to design PMSM of even higher efficiency. In the future, PMSM with high efficiency may have more share of the market once the cost goes down. In summary, PMSM can achieve better performance than other types of machines such as efficiency, power density, weight, maintenance, durability, etc.

There are a lot of research of the machine design on hybrid energy automotive applications. Hybrid energy vehicle contains both an internal combustion engine which is powered by the gas or diesel and an electric motor which is powered by the battery. It depends on the specific type of car that switch the power back and forth between the motor and the engine. However, all hybrid energy vehicles alternate the power between the fuel and the battery. The big advantage is that they

consume less gas than the traditional gas-only driven vehicles. Therefore they produce significantly fewer polluting emissions. Unlike all-electric vehicles, the hybrids still need to be charged mostly by the combustion engine. However, large hybrid vehicles are not as energy efficient as smaller vehicles. Thus, we rarely see large size of hybrid cars in the market. There are different types of machines that people design for hybrid energy vehicle such as switch reluctance motor, DC motor, permanent magnet motor, etc. Control methods for each type of the motors are different [37] - [52]. Electric energy used as the driven power has an obvious shortage that the power stored in the battery is always limited so that the maximum mileage an electric car can drive is not comparable to a traditional car. People try to design the battery with new technology which is able to store more power. Besides, increasing the efficiency of the energy conversion device, which is the motor system, is another way to improve the electrical car to make it comparable to a traditional gasoline car.

In the next two sub-sections, we will start with the research motivation, then move on to the dissertation outline.

1.1 Research Motivation

People are working on improving the design technology of PMSM. Researchers are interested in designing of super compact machines. This is important because the space for the machine system to be mounted into is critical for some applications so that people have to design a machine with small size. Furthermore, with the high-speed achievable, people can make high power rating machines with the same volume since the volume is proportional to the power. Thermal issues have to be considered if the volume of the machine becomes small. In another word, we wish to design a compact machine and have a good solution for the heat dissipation.

By increasing the current density and the air gap flux density, it can contribute to a high power density. However, it also makes the magnetic flux saturation possible which will result

in efficiency greatly reduced. To balance that, we have to investigate on finding high magnetic saturation materials which may lead to high cost. We can also try to better shape the stator teeth in order to reach an optimized peak flux density. Therefore, there are a lot of trade-offs in designing a PMSM. A successful design of PMSM would be the one that can maximize its performance while balances the trade-offs.

The hybrid energy idea on vehicles can be applied to the APU systems. APU is a device that can offer energy for on-board functions other than the propulsion for aircraft, ships, large land vehicles, etc. In the US, no-idle regulations in many jurisdictions require commercial truck drivers to shut off main truck engines during meal times, deliveries and mandatory rest stops, especially during a 10-hour period of air conditioning (at 10,000 BTU's) or heat overnight. Thus, APU powers air conditioner, TV, laptop, microwave and other personal amenities overnight and other times without idling the main engine. Furthermore, the fuel require to run the APU is far less than that used to run the main engine for the same amount of time so that both the economical cost and air pollution can be significantly reduced. In addition, the lifetime of the main engine will be extended due to the use of the APU system [53] - [63]. Most common APUs for a commercial truck rely on diesel or other fossil fuel powered units. Their use is considered idle reduction, not idle elimination. However, all-electric APUs with innovative technology can reduce the fuel usage in commercial truck, and potentially have the ability of saving more than $2 million annually [64]. The APU uses highly efficient lithium-ion batteries instead of the diesel engine as a source of power. Together with a high efficiency motor, the APU can power up to 2,000 watts for 10 hours overnight. Therefore, drivers do not necessarily have to find a truck service stop for electric power. Some practical limitations also restrict the flexibility of some truck operations. Besides, truck drivers may also reject using the service stop for safety reasons. The batteries are recharged whenever the truck is operating. As we discussed earlier, the fuel cost should be an important factor considered as well as the polluting emissions issue. Consequently, idling elimination can be achieved by using all-electric APU systems. Effective use of all-electric APUs is a very important

research area.

In this dissertation, the goal is to explore a novel design methodology of a high efficiency PMSM and implement the design technology into a prototype. A sensorless controller with the field oriented control scheme and sliding mode observer algorithm for this PMSM is developed and tested. Eventually, a system including the PMSM, drive hardware and its supporting devices help to make the all-electric APU a reality.

1.2 Dissertation Outline

The first chapter has presented the history and development of the research on electric machinery. It went over the research background including both the previous and current work on electric machine design as well as the most popular topologies of various motor types. And, we proposed the research motivation in this dissertation. Chapter 2 details the fundamentals of the motor concepts, the design methodology of PMSM and key procedure of a design. Chapter 3 introduces a 12-slot, 10-pole PMSM design for an APU application. Simulation results based on the finite element analysis (FEA) are provided. Chapter 4 discusses the control principle and methodology for this designed motor and its inverter design. A controller prototype is presented as well as the test results. Chapter 5 introduces the design of a permanent magnet motor capable of operating at wide temperature range from -196 °C up to 300 °C. We present the specific design considerations for such special requirement on temperature. Chapter 6 summarizes the contributions of the research.

CHAPTER 2: DESIGN METHODOLOGY OF PERMANENT MAGNET SYNCHRONOUS MOTOR

2.1 Introduction

As it was discussed in the previous chapter, PM motor has many advantages in comparing to the other machines with rotor that requires electromagnetic excitation. It results in the elimination of the copper loss on the rotor, easy maintenance and high power density. In a PMSM structure, stator windings are multiple copper wires wrapped around the tooth for various of winding configurations. The winding configuration will play an important role in the motor performance. Volumetric occupation of some supporting subsystems is reduced by high power density PMSM. However, on the other hand, thermal management becomes a challenge as the volume decreases. There will be a balance among the volume, thermal solution, efficiency, etc.

In this chapter, PMSM concepts are reviewed. A key design methodology is presented. We introduce how to start a design with the design specification in hand. We discuss the design of the stator, rotor, permanent magnet, winding, shaft, housing, etc. Besides, We present the most popular materials and their characteristics for machine design applications. We also discuss the importance of the winding configurations and introduce how to determine the coil pitch and the winding sequence. And, we discuss the power losses and introduce the best loss control for various machine designs. Lastly, computer aided design (CAD) is introduced and it will be applied to confirm and optimize the designs in Chapters 3 and 5, separately.

2.2 Key Design Procedure of PMSM

A complete design procedure of PMSM can be summarized as shown in Fig. 2.1. The design begins with a specification with all the desired parameters such as the rotor rotational speed, terminal bus voltage, output power, efficiency, volume requirement, cost, etc. There are a lot of trade-offs among those design parameters. In another word, some performances can be achieved by reducing the priority level of the other parameters. Therefore, it may not have an unique solution for motor design because it depends on what are the most critical parameters in a specific design.

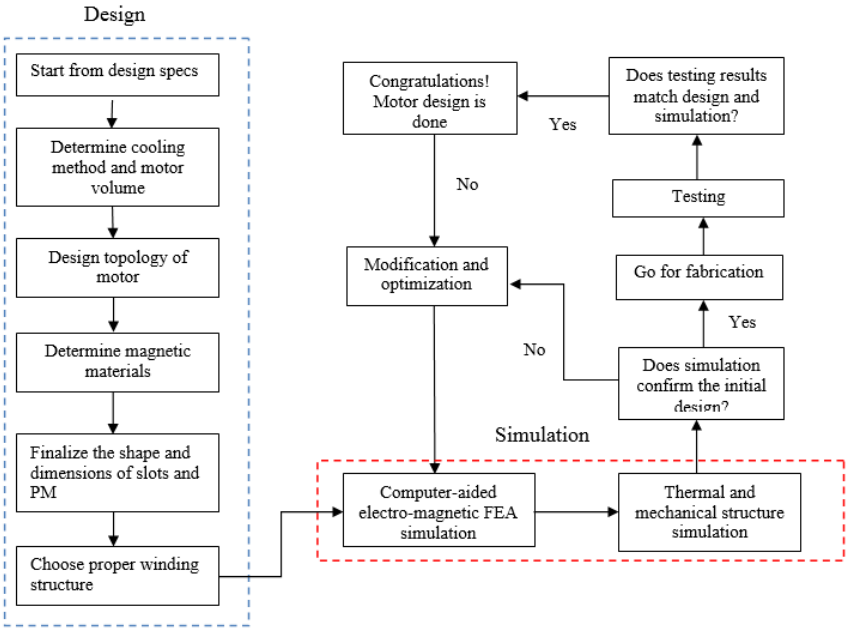

Figure 2.1: PMSM design flowchart.

We have created our own PMSM motor designer by MATLAB. The basic size of the machine can be determined based on the power level, rotating speed and cooling coefficient. Liquid and air cooling are popular. The motor topology, such as the number of slots and poles can be decided. We choose the materials for the stator, rotor, permanent magnet, shaft, etc. The design

detail of the slot and permanent magnet is one of the design steps as illustrated in Fig. 2.1, it will affect the performance, such as flux density, cogging torque, etc. With the stator and rotor designs completed, we can decide the winding structure [65] - [77].

After the motor initial design is basically finished, it has to be confirmed by the electromagnetic simulation using FEA since FEA is good at analyzing electromagnetic variation and distribution. It can provide a detail analysis on the performance of the PM motor [78] - [90].

Thermal analysis and mechanical analysis need to be done to confirm that not only the design meets the requirement from the electrical point of view but also meets the mechanical standard [91]. In summary, the motor design process involves iterative FEA analysis for the electromagnetic, thermal and mechanical performances. An optimum design has to consider all of these design criteria.

Adjustment and optimization are necessary to obtain a better performance if the simulation results are not acceptable. Therefore, some design steps in Fig. 2.1 need to be repeated until we get the desired performance.

2.3 Design of Physical Dimensions

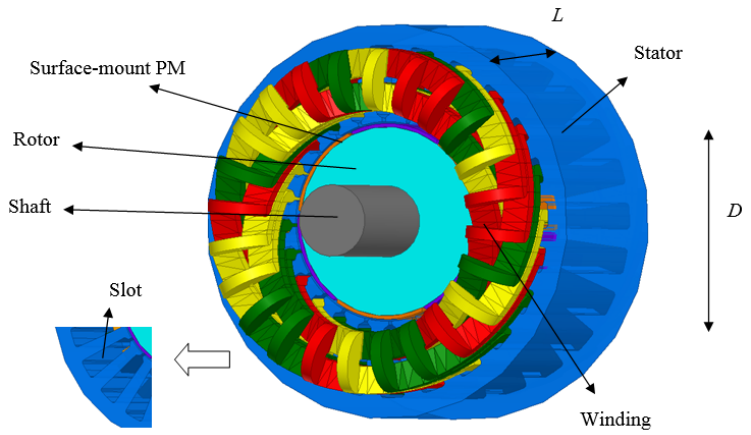

Figure 2.2: 3D Structure of the PMSM.

A high performance PMSM structure is shown in Fig. 2.2. It is mainly made up of a stator with windings, a rotor with surface-mounted permanent magnets and a shaft.

2.3.1 Volume of Machine

The general sizing of the motor can be determined from

$$\begin{aligned} \frac{D^2 L}{T_e} &= V_o, \\ T_e &= \frac{P}{\omega} \end{aligned} \tag{2.1}$$

where D is defined as the stator inner diameter and L is the length of the machine as shown in Fig. 2.2. The torque is represented by T_e, which is determined by the required output power P and the rotor rotational speed ω in rad/s. Therefore, the volume of the machine is inversely proportional to the speed, and is directly proportional to the output power. V_o is a coefficient and depends on the cooling method. Typically, V_0 is around 5 - 7 $\text{in}^3/(ft{\cdot}\text{lb})$ for 10 hp output power

or less with air cooled. While, V_o is around 2 - 5 $\text{in}^3/(ft{\cdot}\text{lb})$ for 10 hp output power or more with water or other liquid cooled. Generally, the size of the motor would be smaller if better cooling is applied. Otherwise, it needs to be designed in such a larger size for adequate heat dissipation. The importance of Eqn. 2.1 is to determine a proper size of the machine based on the design specifications as well as meeting the thermal requirement. Another assumption to be made is that the length of the machine is equal to the inner diameter, i.e. D equals L. This should work fairly well unless there is a special requirement of either the height or length of the machine. If the diameter is much larger than the length, it will cause the motor to have high inertia. On the other hand, if the motor length is much larger than the diameter, bearing and rotor-dynamics could become issues.

2.3.2 Design of Slot

Power input of the three-phase stator windings can be calculated according to an estimation of efficiency. For PMSMs, the efficiency can be greater than 90% and even higher on large power rating machines. With the estimated efficiency and rated output power, we can get the estimated input power. The power input can be expressed as

$$P_{in} = 3V_\phi I_A cos\theta, \tag{2.2}$$

where V_ϕ represents the phase voltage, I_A is the phase current, and θ stands for the power angle.

Current density J_s is also a key factor of the current rating. This determines how the stator slot is designed [92]. In addition to the space that conductors occupy in the slot, sufficient area for cooling is important. Thus, based on the calculation of the wire gauge and the thickness of the insulation around the wire, it is necessary to create extra room for cooling.

The next step is the slot design. There are several types of the slot structure. We use our own PMSM designer to generate a basic dimensional image of the slot. Slot pitch τ_s can be defined

as

$$\tau_s = \frac{\pi D}{S}, \tag{2.3}$$

where S represents the number of the stator slots. The detail design of the stator slot can be developed based on the slot pitch. The structure of the stator slot is shown in Fig. 2.3. Variation on the slot dimensions as shown in Eqn. 2.4 can affect the motor performance such as efficiency, air gap flux density, cogging torque, flux path, machine weight, etc.

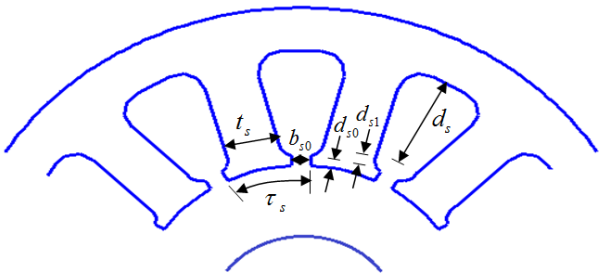

Figure 2.3: Stator slot.

$$\begin{cases} t_s \approx (0.4 - 0.6)\tau_s \\ d_s \approx (3 - 7)t_s \\ b_s = \tau_s - t_s \\ b_{s0} \approx (0.1 - 0.5)b_s \\ d_{s0} \approx (0.1 - 0.5)b_s \\ d_{s1} \approx (0.1 - 0.5)b_s. \end{cases} \tag{2.4}$$

2.3.3 *Design of Air Gap*

For a rotor with multi-pole surface-mounted magnets as shown in Fig. 2.4, according to the magnetic circuit analysis, we have

$$2H_g g + 2H_m d_m = 0, \tag{2.5}$$

where H_g represents the air gap magnetic field, H_m represents the PM magnetic field, g is the air gap size and d_m is the magnet thickness. Further we have

$$\frac{d_m}{g} = -\frac{B_m}{\mu_0 H_m}\frac{k_l A_m}{A_g}, \tag{2.6}$$

where B_m stands for the magnetic flux density of the PM, A_m is the cross section area that the magnetic field passes the PM, A_g is the area that the magnetic field passes the air gap, k_l represents a leakage coefficient and μ_0 is the permeability of free space. We will use the equation shown above to decide the relation between the air gap size and the PM thickness.

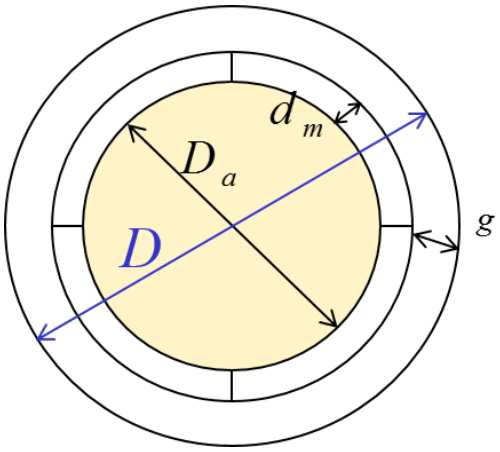

Figure 2.4: Rotor with multi-pole surface-mounted magnets

B_m can be estimated by multiplying the residual flux density B_r by a coefficient α_m. Typ-

ically, α_m is picked up to be in the range of 0.6 to 0.95. The torque angle δ for PMSM is usually designed to be in the range of 15-30 degrees (20 degrees is a common value). We design a torque angle in the range of 2-15 degrees for more power handling capability. It leads to Eqn. 2.7, which the peak value of the net magnetic field $B_{g,pk}$ and peak winding magnetic field $B_{a,pk}$ are defined:

$$\begin{aligned} B_{g,pk} &= B_{r,pk}cos(\delta) \\ B_{a,pk} &= B_{r,pk}sin(\delta), \end{aligned} \tag{2.7}$$

where the peak air gap magnetic field, $B_{r,pk}$, is calculated by

$$B_{r,pk} = \frac{4}{\pi}\sin(\frac{\rho_{pm}}{2})B_m, \tag{2.8}$$

where the electrical angle of the permanent magnet, ρ_{pm}, can be calculated by

$$\rho_{pm} = e_m\pi, \tag{2.9}$$

where e_m represents the embrace of the permanent magnet. It can be varied from 0.5 to 1. The variation will mainly tell how efficient the permanent magnet can be utilized and how much it contributes to the air gap magnetic field. Besides, the variation can also affect the peak flux density of the teeth and yoke, cogging torque, etc.

Previously, in order to calculate the air gap size, Magnetic Magneto Force (MMF) was simply represented by multiplying the total flux of the air gap by the length of the air gap. However, it will not be accurate if the designed air gap is large such as in PMSM design. Therefore, we analyze the mathematical model of the air gap and express the MMF by a logarithm function, from which we can determine the air gap size more accurately. The calculation of the air gap size is derived according to Fig. 2.5. Thus, MMF that generated from the permanent magnet, F_{pm}, can

be found by the equation below:

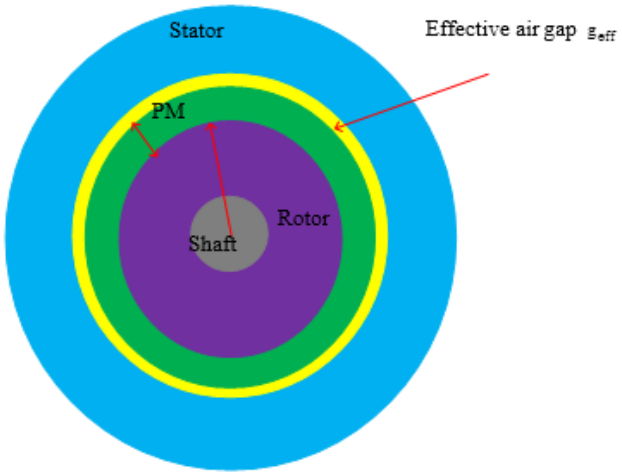

Figure 2.5: Air gap modeling

$$F_{pm} = \int_{r_a}^{r_a+d_m} H_m(r_m)dr_m = \frac{\Phi_m}{2\pi L\mu_0\mu_{rm}} \ln\left(\frac{r_a+d_m}{r_a}\right), \tag{2.10}$$

where Φ_m is the flux of the permanent magnet, r_a represents the inner radius of the rotor, and d_m represents the thickness of the permanent magnet. The MMF that generated from the air gap, F_{gap}, can be found as

$$\begin{aligned} F_{gap} &= \int_{r_a+d_m}^{r_{is}^{'}} H_g(r_g)dr_g = \frac{\Phi_g}{2\mu_0} \ln\left(\frac{r_{is}^{'}}{r_a+d_m}\right), \\ r_{is}^{'} &= r_a + d_m + g_{eff} \end{aligned} \tag{2.11}$$

where Φ_g is the flux of the air gap, and g_{eff} represents the effective air gap size. For any given machine, Φ_g almost equals Φ_m. Therefore, the total MMF from the two parts can be added up and expressed by

$$
\begin{aligned}
F_{total} &= \frac{r_g B_{r,pk}}{\mu_0}\left[\frac{1}{\mu_{rm}}\ln\left(\frac{r_a+d_m}{r_a}\right)+\ln\left(\frac{r_{is}^{'}}{r_a+d_m}\right)\right], \\
r_{is}^{'} &= r_a + d_m + g_{eff}
\end{aligned}
\tag{2.12}
$$

where r_g is the radius of the actual air gap. Then we can get g_{eff}. With the effective air gap size known, we can get the actual air gap by

$$
\begin{aligned}
g &= (1-\alpha_m) g_{total}^{'}, \\
g_{total}^{'} &= \frac{g_{eff}}{k_c}
\end{aligned}
\tag{2.13}
$$

where k_c is the Carter$^{'}$s coefficient. We need to pay attention that the size of the air gap is also dependent on the motor's operating speed because high speed will generate big windage friction in the air gap area which will cause annoying noises even if the design of the air gap is reasonable from the electrical point of view.

Ideally the power angle θ should be zero, which means the power factor $cos\theta = 1$, as shown in Fig. 2.6. The phasor diagram can represent the relation among the phase voltage V_ϕ, induced voltage E_A, and voltage drop on the winding jX_sI_A. Besides, the phasor diagram can also represent the relation among $B_{r,pk}$, $B_{a,pk}$, and $B_{g,pk}$.

However, in actual design, it is hard for the power factor to be exactly equal to 1. We normally design it to be 0.95, which leads to $cos\theta$ = 0.95, the phasor diagram for the motor operates at underexcited mode is in Fig. 2.7 and overexcited mode in Fig. 2.8, respectively.

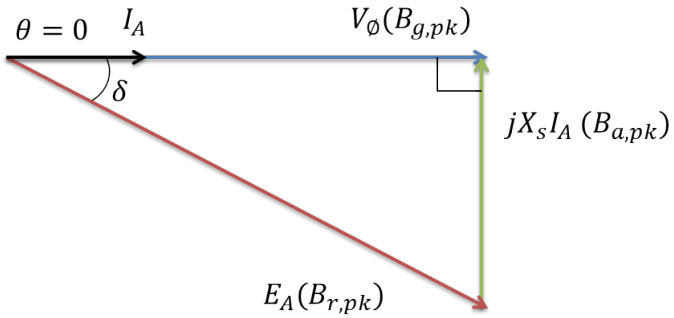

Figure 2.6: Phasor diagram for power angle = 0

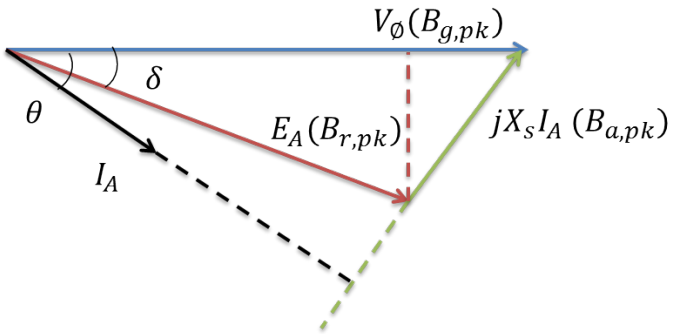

Figure 2.7: Phasor diagram for underexcited mode

2.3.4 Design of Permanent Magnet

The thickness of the surface-mounted permanent magnets, d_m, can be calculated by

$$d_m = \alpha_m g'_{total} \mu_{rm}, \tag{2.14}$$

where μ_{rm} is the permeability of the permanent magnet material. The length of the permanent magnets in the axial direction usually can be the same as the length of the rotor, unless special requirements are proposed. Typically, the force that the permanent magnets can provide is directly

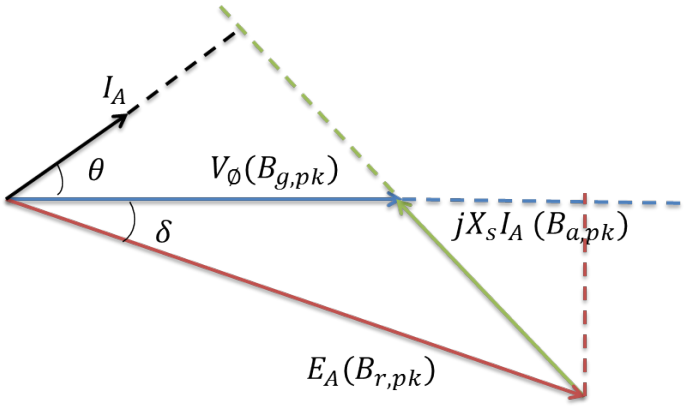

Figure 2.8: Phasor diagram for overexcited mode

proportional to the amount of usage of the permanent magnets. However, rare-earth permanent magnet materials are expensive in the market, we will therefore optimize the usage of the permanent magnet in order to control the overall cost.

2.3.5 Design of Rotor, Shaft and Housing

Eventually, we can get the outer diameter of the rotor:

$$D_r = D - 2g. \tag{2.15}$$

However, there is a minimum requirement for the diameter of the shaft, D_{sh}, due to the maximum stress limit that the shaft can handle. The stress capability coefficient, τ_{max}, depends highly on the material of the rotor, resulting in

$$D_{sh} = \sqrt[3]{\frac{2T_e}{\pi\tau_{max}}}. \tag{2.16}$$

Furthermore, there is also a limit for the maximum rotor diameter allowed which is calculated from the maximum peripheral speed of the rotor. It may be possible that with certain

peripheral speed, the tip speed might even reach sonic speed level if the radius of rotor is large enough, resulting in structure failure. The maximum allowed tip speed is 250 $\mathrm{m/s}$ in this design.

Lastly, a neat housing should be designed to encase the machine, which can prevent dust, water, etc. In addition, it can also be used as a powerful heat sink. A good housing with a high thermal dissipation capability can be equivalent to a design with a smaller cooling coefficient V_o being introduced in Eqn. 2.1. It should be pointed out that the total end-turn length on both sides of the winding may reach up to the length of the stator itself. Therefore, we need to design the housing with enough room in the axial direction to cover the end-turn windings.

2.4 Material Selection

The performance of the electrical and magnetic materials depends highly on the operating temperature. Many materials are subject to degradation of performance with an increase in temperature. Therefore, to demonstrate that the designed permanent magnet motor can work in the entire operational temperature range, the motor must meet all the specifications at the worst-case scenarios. Thus, material selection for the stator and rotor core, windings, and permanent magnets are most critical in determining the performance of the motor [93] - [97].

Since Neodymium Iron Boron (NdFeB) is the strongest rare-earth material, it is popular to be used as the permanent magnet material. However, the suggested operating temperature for NdFeB is only $150\,^{\circ}\mathrm{C}$ thus will weak the performance at temperatures above $150\,^{\circ}\mathrm{C}$. Other good materials such as Samarium Cobalt (SmCo) can work up to $350\,^{\circ}\mathrm{C}$. We will have SmCo being applied to a design of PM motor with wide temperature in Chapter 5.

Soft magnetic materials such as steels usually saturate at magnetic flux density of 1.7 tesla (T), and have poor performance at higher temperature. For motor design applications which will not exceed $100\,^{\circ}\mathrm{C}$, we use steel as the stator and rotor materials. However, for machines that need to run with a higher temperature, Hiperco50, which is an iron cobalt vanadium soft magnetic

alloy, is used as the soft magnetic material. It exhibits at high magnetic saturation around 2.3 T, high DC maximum permeability, low DC coercive force, and low AC core loss. Higher magnetic saturation results in the ability to reduce the rotor and stator volume and reduce the iron core loss, thus increasing the efficiency and power density. Hiperco50 can stand a temperature up to $350\,^{\circ}$C. In Chapter 5, we will use Hiperco50.

Stator windings are made of copper, therefore it is important to consider the dependence of the resistivity of the copper on temperature. As temperature increases, resistivity increases, resulting in an increase in resistance in the winding. Copper loss of the motor goes up as temperature increases. In addition, copper windings generally have an operating temperature limit of $200\,^{\circ}$C maximum with regular insulation materials. Insulation materials deteriorate and fail primarily due to high temperatures. Thus, for other motor applications which will run in a higher temperature environment, special materials such as ceramic fiber with higher heat tolerance will be applied. It can work at a temperature up to $700\,^{\circ}$C. It costs more compared to the regular insulation.

2.5 Design of Winding Configuration

Windings of the PMSM refer to the copper wires in the stator slots. The input of the motor is three-phase AC voltages. There are numerous ways to configure the winding in a PM motor such as single-layer lap winding, double-layer lap winding, concentric winding, etc. Various winding structures will have effect on the flux linkage, inductance, MMF, etc. [98]. Flux linkage and inductance are the fundamental concepts of the stator winding. The flux ϕ is represented as

$$\phi = \frac{NI}{R}, \tag{2.17}$$

where N represents the number of turns, I is the current, and R describes the reluctance. Therefore, the flux linkage λ can be defined by

$$\lambda = N\phi. \tag{2.18}$$

Once the shape of the slot is determined, the number of the conductors per coil N_c is calculated by using

$$N_c = \frac{1.1V_\phi}{2\sqrt{2}\pi f_e q k_w B_{g,pk} DL}, \tag{2.19}$$

where V_ϕ represents the phase voltage, f_e is the electrical frequency, q describes the number of the winding groups per pole, and the winding factor is given by k_w, it varies with how the wires are wounded around the teeth [99] - [104]. Similarly the effective turns per phase is calculated by

$$N_{eff} = \frac{pqN_c k_w}{1.1}, \tag{2.20}$$

where p refers to the number of poles. In addition to the number of turns per coil, we also need to know the coil pitch in order to wind the wires. The method introduced in the following can help to determine the coil pitch. It can be divided into several steps.

Step 1: Find the nominal coil span in slots. If S/p is an integer, we have

$$S_c = \frac{S}{p} - 1. \tag{2.21}$$

However, if S/p is NOT an integer, we have

$$S_c = max(fix(\frac{S}{p}), 1). \tag{2.22}$$

Step 2: Calculate the relative electric angle of "in" slot of all coils. The relative electrical angle (expressed in the range of -180 ° to 180 °) of the kth slot is

$$\theta_{slot}(k) = mod[(k-1)\gamma + 180\,^\circ, 360\,^\circ] - 180\,^\circ, \tag{2.23}$$

and

$$\gamma = \frac{p}{2}\frac{360^\circ}{S}, \tag{2.24}$$

where γ stands for the slot pitch. And, the relative electrical angle of "in" slot of the kth coil is

$$\theta_{coil}(k) = mod[(k-1)\gamma + 180^\circ, 360^\circ] - 180^\circ. \tag{2.25}$$

Step 3: Re-adjust "in" slot angles if their magnitude are greater than 90°. For coil angles who have a magnitude greater than 90°, the coil direction will be reversed; thereby simply changing the angle by 180° should get you a correct angle.

Step 4: Picking up (S/m) coils for Phase A. For the angles calculated in the last step, pick up those (S/m) close to 0° as phase A coils for convenience.

Step 5: Calculate the slot offset to wind the other phases. From Eqn. 2.24 and Eqn. 2.26, we can derive Eqn. 2.27.

$$mod[S_{off}\gamma, 360^\circ] = \frac{360^\circ}{m}. \tag{2.26}$$

$$S_{off} = 2\frac{S}{mp}(1+mn) = 2q(1+mn), \tag{2.27}$$

where n is an integer that makes S_{off} also an integer. From the calculated S_{off}, we can have an idea where to wind phase B, which is from the slot (mod($S_{off}, S) + 1$).

Step 6 (final step): Confirm the winding is valid. The winding will be considered as valid if all slots contain two coil sides each. If it can not pass the validity check, go back to Step 4 and pick up more appropriate coils for phase A.

By following the method discussed above, we can make a good winding scheme based on the combination of the number of slots and poles. Since it will increase the difficulty of hand-winding, we normally choose a suitable wire gauge so that the slot fill factor will not exceed 85%.

Furthermore, we can simulate the winding setup by the computer aided design tool to compare with the analytical results.

2.6 Power Losses

Power loss is important to be evaluated to know the motor performance. The efficiency primarily depends on the copper loss, iron core loss, bearing friction loss, windage loss, etc. Bearing friction loss typically is very small, it can be ignored compared to the other losses in most cases. The copper loss can be calculated by

$$P_{copper} = 3I^2R, \tag{2.28}$$

where

$$\begin{aligned} R &= \rho\frac{l}{s}, \\ \rho &= \rho_{ref} + \alpha_T(T - T_{ref}) \end{aligned} \tag{2.29}$$

where ρ represents the resistivity of the copper, and α_T is a temperature coefficient. Other losses from the windings can be called stray losses. They can be generated from the skin and proximity effects. Specifically, in skin effect, the density of the current flowing in a conductor tends to migrate toward the surface of the conductor. While, in proximity effect, when conductors are packed together, as they are in the stator slots, induced fields of the individual conductor affect the surrounding conductors packed next to it.

Iron core loss can be subcategories as the hysteresis and eddy current losses. Hysteresis losses are primarily due to the alternating magnetic field passing through the stator core. While, eddy current losses are due to the induced current by alternating magnetic field. The core loss in

total can be represented as

$$P_{core} = k_h B^2 f_e + k_c (B f_e)^2 + k_e (B f_e)^{3/2}, \tag{2.30}$$

where k_h, k_c and k_e are the coefficients of the hysteresis loss, classical eddy current loss and excess eddy current loss, respectively. They depend on the type of the magnetic material, f_e is the electrical frequency, B is the flux density on the soft material and it decreases with the temperature increases due to the demagnetizing phenomenon [94]. It follows the equation:

$$B = B_{c,ref} + \alpha_c (T - T_{ref}), \tag{2.31}$$

where $B_{c,ref}$ is the residual flux density at the reference temperature, α_c is a coefficient and can be chosen in the range of 0.001-0.005. For low speed machine, the copper loss is dominated, unless for high speed applications, calculation of the core loss will become more involved. Choosing the most suitable material for the stator core is critical for the design characteristics. It would be successful to pick the material which can tolerate high flux density saturation in order to decrease the machine volume, weight, losses as well as high permeability for less reluctance. However, there are always trade-offs between the electromagnetic saturation point and the iron core loss consumption. The rotor also experiences loss due to the eddy current effect induced in the shaft and the permanent magnets. Lamination technique is needed for the rotor and stator. Typically, there are several factors that can help reducing those losses such as fractional number of slot to pole ratio, shape of the slot opening, winding pitch, etc.

Windage loss is significant on high speed machine applications. The air property changes at higher temperature. The following method has been used in calculating the windage loss [69].

Firstly, the Reynolds coefficient is expressed as

$$R_e = \omega r l_g \rho_{air} / \mu, \tag{2.32}$$

where r stands for the radius of the rotor, l_g is the length of air gap, ρ_{air} is the air density, and μ represent the air viscosity. Besides, the Taylor coefficient is

$$T_a = R_e (l_g / r)^{0.5}. \tag{2.33}$$

When the Taylor coefficient is very large, such as above 400, it will have a phenomenon called turbulence behavior, and another coefficient C_d is

$$C_d = 0.0095 (T_a)^{-0.2}. \tag{2.34}$$

Eventually, we can derive the final expression of the windage loss, P_w:

$$P_w = C_d \pi \rho_{air} \omega^3 r^4 L. \tag{2.35}$$

As shown in the equation, with a high mechanical speed ω, the windage loss can increase tremendously. However, for low speed operation, the windage loss can be assumed simply by 2% of the total power loss. It is estimated that PMSMs dissipate about 5-10% of the total input power as heat to the ambient. We can choose the nature air cool, or shaft-attached fan, or liquid pipe to manage the thermal issues. They are all popular and efficient ways in thermal management. Test work is necessary to confirm the initial estimation after the motor is fabricated. It is important that temperatures for both the motor and controller device should be under the control. More details about the thermal management for the drive system will be introduced in Chapter 4.

2.7 Computer Aided Simulation

In order to model the machine in computer, we need to extract some parameters from the initial design and build the machine in the software. Some parameters are obtained based on the experience, and for others, they may be either difficult or even impractical to acquire through the experimentation. Therefore, in such cases, the simulation is able to provide accurate information. Furthermore, we use both Maxwell 2D and 3D packages to do the post-design FEA and determine the performance of the machine. The simulation can be very time-consuming. However, it is still worthy to do so. In the next chapter, we will provide the simulation results for a 12-slot 10-pole motor design by Maxwell. In addition, in Chapter 5, we will use Maxwell simulation for a 24-slot, 6-pole motor design.

2.8 Summary

In this chapter, we presented the fundamental theory of designing a PMSM. Based on a design specification, we need to consider the most important parameters for a specific design as opposed to treat all of the parameters as the same priority level. The reason of doing this is because there are always trade-offs in PM motor design that we may have to sacrifice some in order to achieve the others, vice versa. We introduced how to determine the dimensions of the motor using our own analytic tool. We showed the design of the stator slot, air gap, permanent magnet and rotor, etc. We explained the reason that why CAD analysis needs to be included. In addition, we introduced the material selection which depends highly on the actual environment that the motor runs at. We need to choose the material which can operate in a desired ambient temperature, but at a minimum cost. Besides, the principle of the winding setup is discussed as well as the cooling considerations for PMSM. We can follow that methodology to design the winding configuration, and then check the air gap flux distribution in the computer simulation. Adjustments can be made to the winding if the distribution curve is not smooth. The PMSM design procedure

is an iterative process which means re-design would be needed if the performance of the machine from the computer simulation is not acceptable.

In the next chapter, we will implement the design methodology into a 12-slot, 10-pole motor design for an electric APU application.

CHAPTER 3: DEIGN OF A PERMANENT MAGNET SYNCHRONOUS MOTOR FOR ALL-ELECTRIC AUXILIARY POWER UNIT

3.1 Introduction

In the previous chapter, we have described the methodology of how to design a PMSM machine. In this chapter, we apply the methodology to the design for an electric APU application.

Utilization of renewable energy have become the future trend in the trucking industry, which can significantly reduce the usage of fuel. As it was discussed in Chapter 1, there are currently APUs on commercial truck which use a small combustion engine to drive the air conditioner compressor while the truck is parked. However, it still consumes fuel and produces emissions. Our purpose is to design an all-electric APU system which uses electrical power generated from renewable energy to replace the small engine powered by fuel and a high efficiency motor to drive the air conditioner compressor. Therefore, fuel consumption and pollution can be greatly reduced by applying the all-electric APU.

There is usually limited space for storing on-board batteries. People try to improve the technology on the batteries so that they can have more storage capacity for power. On the other hand, to better utilize those batteries, it becomes necessary to have a highly efficient energy conversion device. In this chapter, we design a permanent magnet electric motor that can be used to compete the market of the electric APU products. The designed motor will have an output power of 2 kW at 2 krpm, and maintain a high efficiency greater than 90%. It has to meet the design requirements such as space saving, high efficiency, low noise, etc. The design calls for good performance over a speed range of 1.5 krpm to 2.5 krpm. The automobile air conditioning system currently works by a “on” or “off” mode. For the heat mode, that means it is on with heat once the cabin temperature drops down to a level and off if the temperature rises back above that level. For the cool mode, that means it is on with cold air once the cabin temperature rises above a level,

and off if the temperature drops back to that level. This is because the motor does not have the speed self-control functionality according to the temperature variation and people in the cabin do not feel much comfortable for that temperature change periodically as well as the inefficient energy consumption.

Copper loss is the most significant of all the losses in low speed electric machines. Reducing the copper loss is the key to build highly efficient machine. We use copper wires with the current density lower than the traditional design which result in large cross section of the wire and thus reduce the copper loss and improve the efficiency. The preferred value of the current density is in the range of 3 to 8 $\mathrm{A}/(\mathrm{mm})^2$. This also makes thermal management easier and reduces the need to use active cooling methodologies (such as fan, liquid cooling or spray cooling); and hence the overall power density of the whole system (including cooling devices) may not decrease much. Besides, since the copper loss of the machine is proportional to the current squared, reducing the current is an effective way to reduce the copper loss and improve the efficiency. In practice, the magnetic saturation will be reduced due to the current reduction. The size of the machine depends on the electrical frequency due to the number of turns per coil is inversely proportional to the electrical frequency. Since the electrical frequency is equal to the pole pair multiply by the mechanical frequency, increasing the speed and number of poles will decrease the number of turns per coil which will result in less window areas needed. Therefore the size of the machine can be reduced. For low speed machine, when the mechanical speed is fixed, large number of poles can effectively increase the electrical frequency. Thus, in order to balance back the reduction of the power density, we use 10 poles to boost up the electrical frequency and thus reduce the number of turns per coil. In traditional machine design, the torque angle is in the range of 15 to 30 degrees at the rated power and speed. In our high efficiency motor design, we use much lower torque angle of 2 to 15 degrees at the rated power and speed. Design with small torque angle can effectively increase the overload power handling capability and efficiency. Besides, small torque angle will result in large airgap and large thickness of the permanent magnets. Large airgap helps to reduce the windage loss of

the machine and generates less noise based on our motor design experience. Large thickness of the permanent magnets also helps to avoid the demagnetization issue.

With our novel technology, the designed motor can adjust its speed through the embedded system of our novel DC to AC inverter to provide a variable load. For example, with high efficiency, the fully charged battery set (48 volts) can supply the electrical power and cooling to the cabin for about 10 hours without recharging using the main engine. The design exploits theoretical investigation, empirical data, lessons learned and best practices as well as carefully measured data derived from observation and testing.

In the following sections, we will have an analytical design based on the methodology being discussed in the previous chapter. We will show the results from CAD with finite element analysis to confirm the initial design. The motor system includes laminated stator, rotor, surface mounted permanent magnets, wound stator with electromagnets, housing, and sensorless control system [96].

The rest of the chapter is organized as follows. Design and simulation results will be introduced in section 3.2. The prototype of the designed PMSM will be presented in section 3.3. Finally, we present a summary in section 3.4.

3.2 Design and Simulation Results

The geometry of the designed motor can be viewed, which is a 12-slot, 10-pole fractional pitch design. To avoid the magnetic saturation, we carefully designed the dimensions of the slot as illustrated in Fig. 3.1. We have chosen concentric winding for our design.

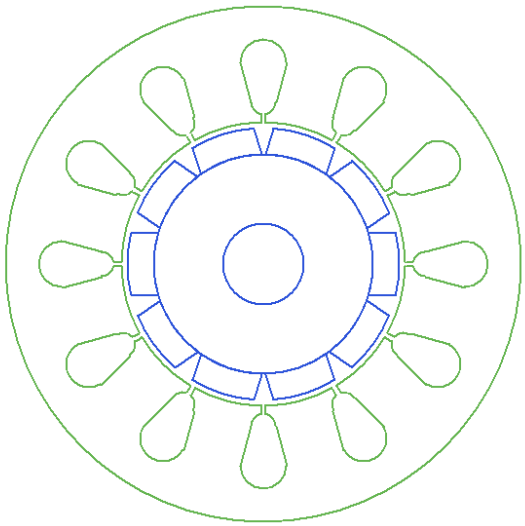

Figure 3.1: Geometry of the PMSM.

The results of the designed motor are summarized in Table. 3.1.

Copper loss is dominated in comparing with the other losses especially in low speed electric machines. The calculation of the copper loss is estimated by

$$P = I^2 R. \tag{3.1}$$

Copper wires with low current density result in large wire diameter which will reduce the copper loss since the copper resistance is inversely proportional to the cross section area of the wire. Although large wire needs more slot area, highly efficient machine generates much less heat. The copper loss of the machine is proportional to the current squared. Reducing the current is an

Table 3.1: Results of the PMSM design.

Machine Type	PMSM
Rated Output Power	2 kW
Rated Voltage	48 V
Number of Poles	10
Number of Stator Slots	12
Outer Diameter of Stator	157 mm
Inner Diameter of Stator	87 mm
Length of Machine	87 mm
Outer Diameter of Rotor	83 mm
Minimum Air Gap	2 mm
Type of Steel	Steel 1010
Type of PM	NdFeB 48
Max. Thickness of Magnet	8 mm
Number of Conductors per Slot	6
Wire gauge	21
Number of wire in each strand	60
Stator Slot Fill Factor	73%
Total Machine Weight	11.2 kg
Efficiency	>90%

effective way to reduce the copper loss and improve the efficiency.

The magnetic saturation will also be reduced due to the reduced current. Therefore, wide teeth are used to avoid the magnetic saturation even if the machine runs at heavy load as shown in Fig. 3.2. Besides, PMs are marked by the purple and orange colors, representing the north and south poles, respectively. Layers in the slots are also marked by various colors for easy recognition. In addition, we use Litz wire in this design to reduce the skin effect and proximity effect which will eventually contribute to the efficiency improvement. This can also help to reduce the size of the slot opening and hence reduce the current and cogging torque.

Fig. 3.3 shows the actual connection of the three-phase windings in groups. Each turn is wrapped around adjacent slot as the concentric winding structure. In addition, the connection can

also be illustrated in a format of table, as shown in Table. 3.2.

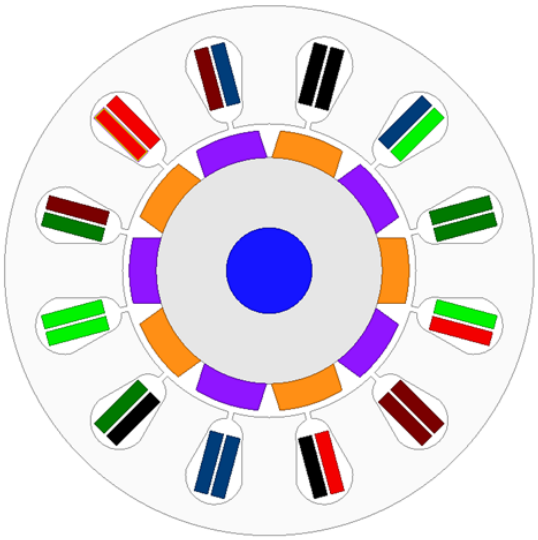

Figure 3.2: Motor geometry.

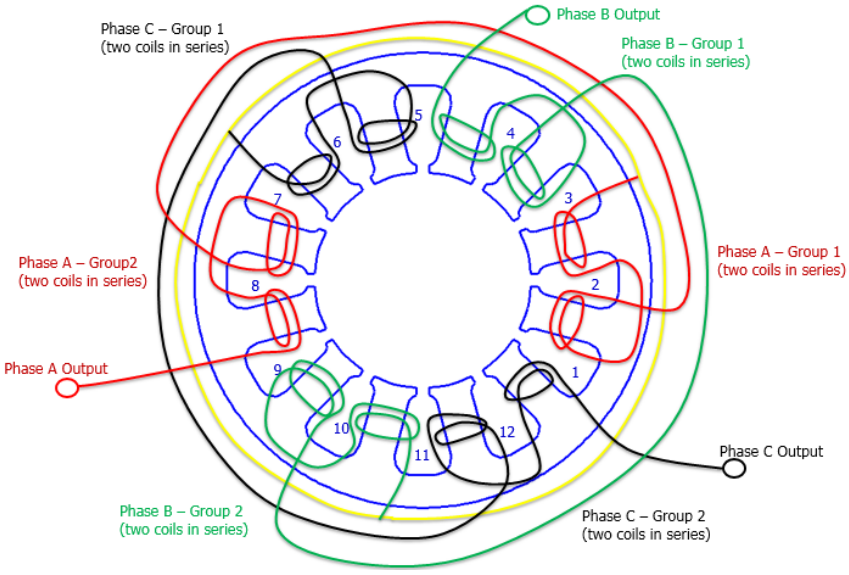

Figure 3.3: Configuration for the concentric winding.

Table 3.2: Winding table.

Slot Number	Phase A	Phase B	Phase C
1	In		Out
2	Out & Out		
3	In	Out	
4		In & In	
5		Out	In
6			Out & Out
7	Out		In
8	In & In		
9	Out	In	
10		Out & Out	
11		In	Out
12			In & In

Until now, the PMSM design is completed. According to the dimensions, we draw a 3D structure of the motor as shown in Fig. 3.4.

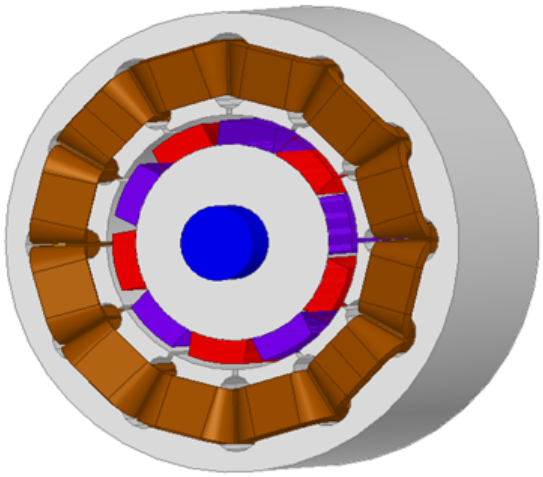

Figure 3.4: 12-slot 10-pole PMSM design.

Fig. 3.5 to Fig. 3.12 illustrate the magnitude distribution of the flux density (**B**) in 3D plot, it varies as the rotor rotates to a position of 45 degrees, 90 degrees, 135 degrees, 180 degrees, 225 degrees, 270 degrees, 325 degrees, 360 degrees, respectively. From the results, we can monitor the peak flux density while the motor is operating. The "rainbow" legend tells where the highest density is located at. We need to make the peak density under the control in order to avoid the magnetic saturation. The average magnitude distribution of the flux density (**B**) meets the property requirement of the soft material we used.

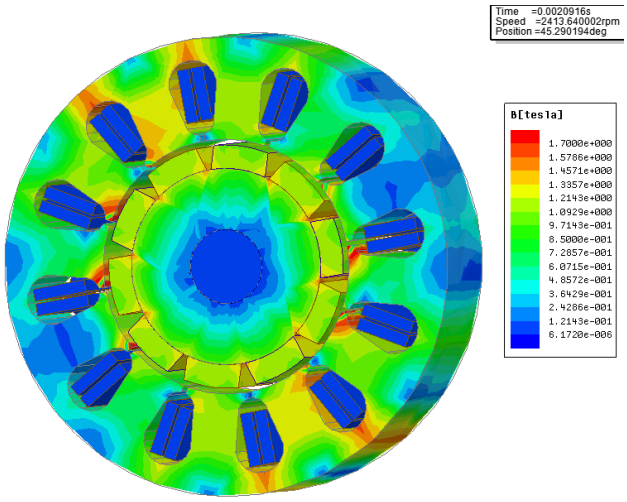

Figure 3.5: Magnitude distribution of the flux density (**B**) with rotor rotates 45 degrees.

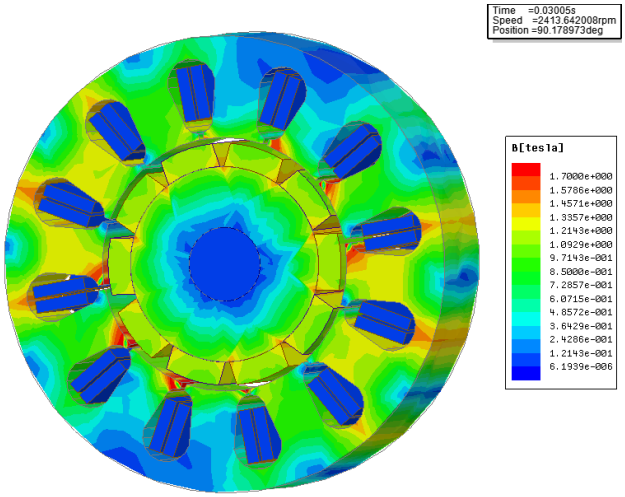

Figure 3.6: Magnitude distribution of the flux density (**B**) with rotor rotates 90 degrees.

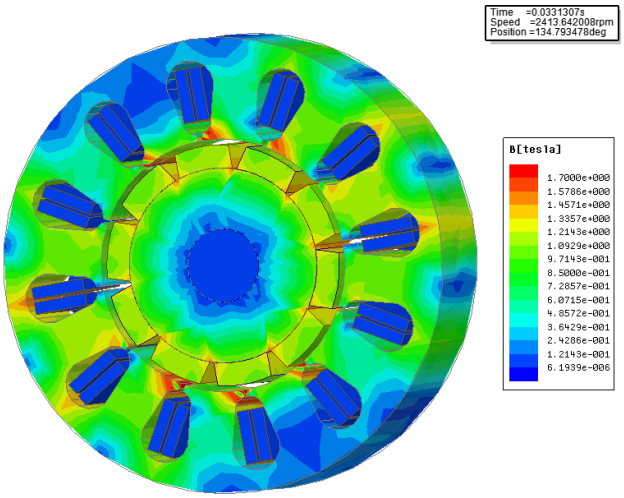

Figure 3.7: Magnitude distribution of the flux density (**B**) with rotor rotates 135 degrees.

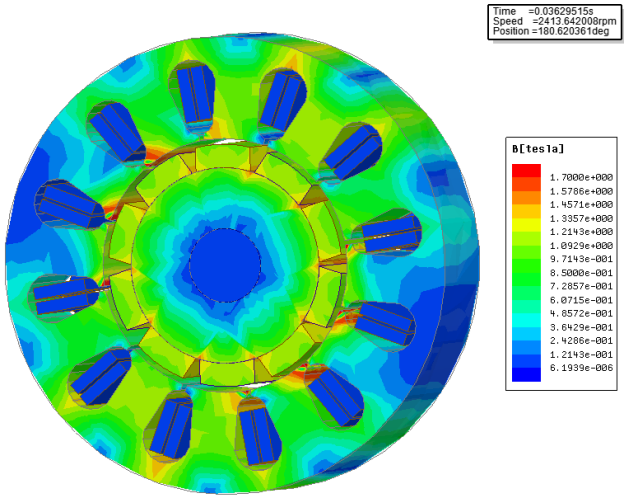

Figure 3.8: Magnitude distribution of the flux density (**B**) with rotor rotates 180 degrees.

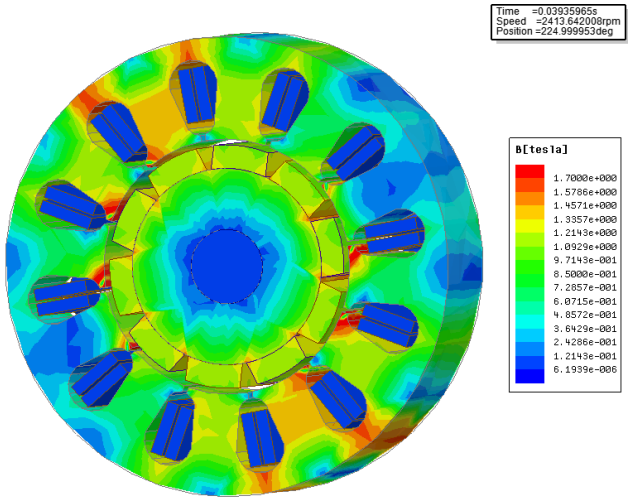

Figure 3.9: Magnitude distribution of the flux density (**B**) with rotor rotates 225 degrees.

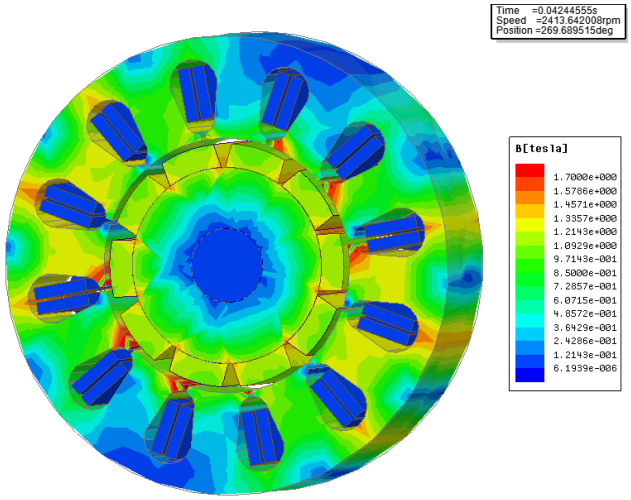

Figure 3.10: Magnitude distribution of the flux density (**B**) with rotor rotates 270 degrees.

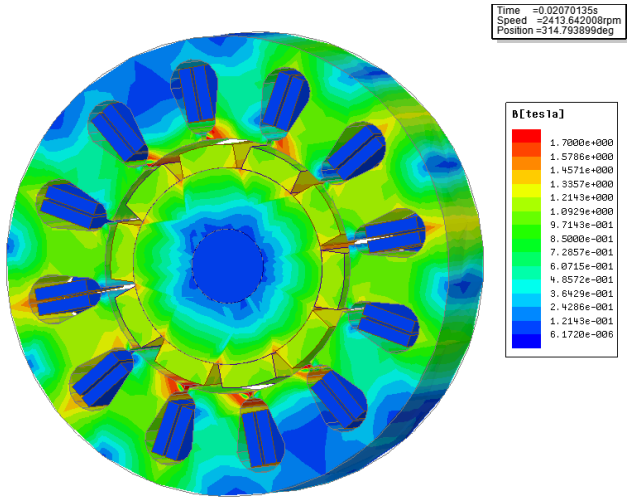

Figure 3.11: Magnitude distribution of the flux density (**B**) with rotor rotates 315 degrees.

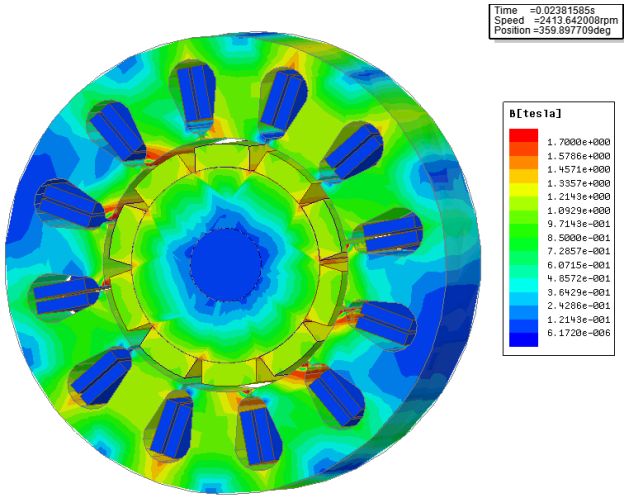

Figure 3.12: Magnitude distribution of the flux density (**B**) with rotor rotates 360 degrees.

The air gap flux density distribution is shown in Fig. 3.13. As we have discussed in Chapter 2, for a good design, the waveform of the flux density should be close to a sinusoidal distribution.

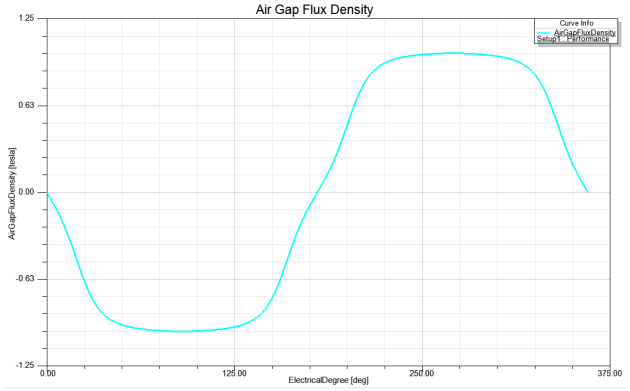

Figure 3.13: Air gap flux density.

The motor's winding currents from the simulation can be seen in Fig. 3.14. The value of the AC winding current is an important factor for the inverter design to ensure that the controller can hold that amount of phase current at full load. The winding flux linkages are shown in Fig.

3.15. They are designed to be a sinusoidal distribution with harmonics and the simulation result proves that.

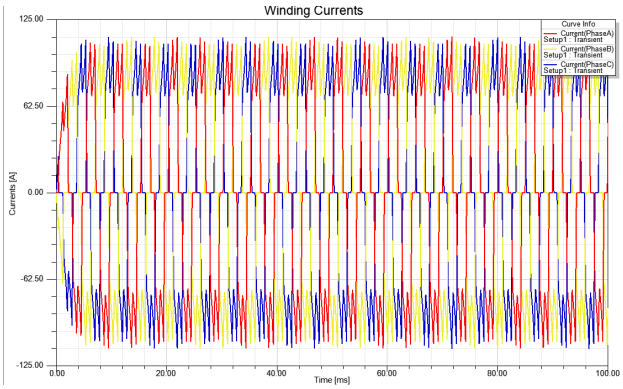

Figure 3.14: Winding currents.

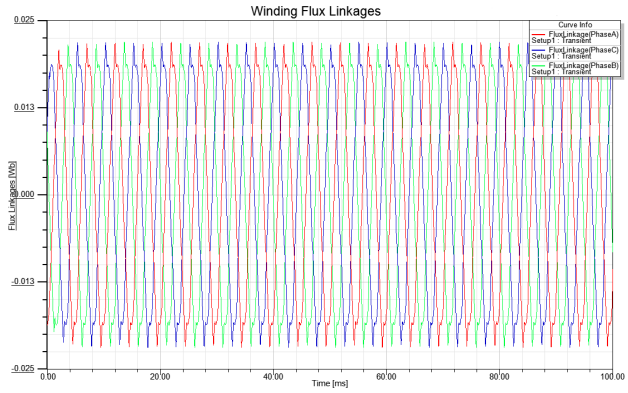

Figure 3.15: Winding flux linkages.

In addition, the three-phase induced voltages are presented in Fig. 3.16.

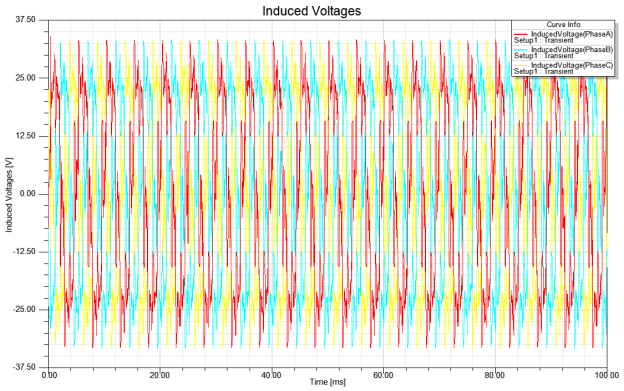

Figure 3.16: Winding induced voltages.

3.3 Motor Prototype

In the previous section, the design was finalized and we are going to discuss the fabrication process of the motor in the following. By using the lamination technique, the core loss of the motor can be significantly reduced. The lamination layers are stacked together for the stator and rotor as shown in Fig. 3.17. We can see that the wide tooth structure is applied to the design.

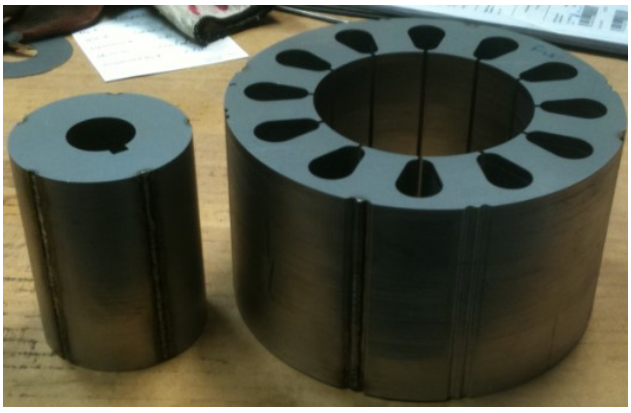

Figure 3.17: Stator and rotor lamination.

The concentric winding structure is shown in Fig. 3.18. As we discussed how to select a proper coil pitch in Chapter 2, concentric winding is a good option for this 12-slot and 10-pole machine. It will have less end-turn length, less cogging torque, better efficiency, etc.

The fabricated stator with the winding assembly and the motor with housing can be viewed in Fig. 3.19 and Fig. 3.20, respectively.

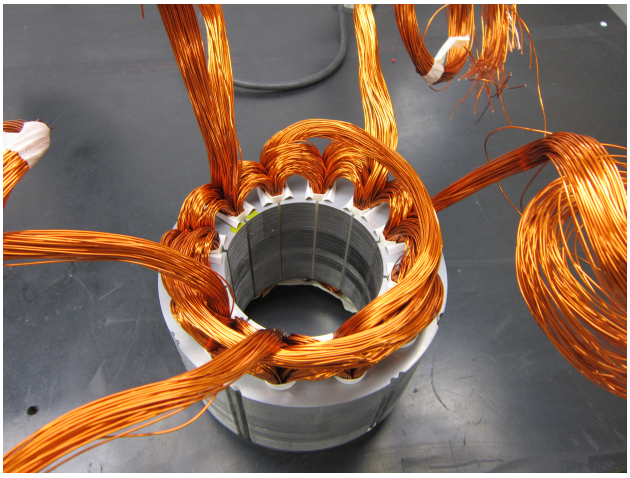

Figure 3.18: Winding.

Figure 3.19: Stator of the motor.

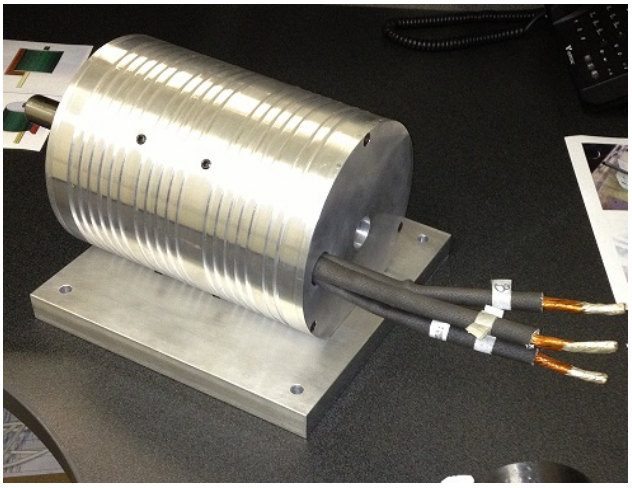

Figure 3.20: Motor with housing.

The test work of the designed motor will be carried out with the controller in Chapter 4, Section 4.6.

3.4 Summary

The research motivation and target of the design have been introduced. We have successfully developed a PMSM as an energy conversion device for a truck all-electric APU application. We chose to use a 12-slot, 10-pole topology with surface-mounted permanent magnets and a concentric winding scheme. The designed motor has an output power of 2 kW at 2 krpm, and is able to reach the efficiency greater than 90%. The use of the permanent magnets as the main magnetic field can help to save the electrical energy and reduce the carbon footprints as well as requiring less maintenance while providing improved reliability. Small torque angle has been applied to increase the overload power handling capability and efficiency for this motor. We have provided the design and simulation results, which show the key characteristics and performance of the motor. Besides, we also fabricated a motor prototype based on our design data for test.

CHAPTER 4: DRIVE SYSTEM DESIGN FOR PERMANENT MAGNET SYNCHRONOUS MOTOR

4.1 Introduction

Traditionally, synchronous motors use rotor windings to generate the rotor flux. The contact between the rotor and stator windings are commutator segments. To improve the drawbacks of maintenance needs and less reliability issue of the brushes, the rotor windings can be replaced by permanent magnets. The interaction between the stator and rotor magnetic field produces a torque and we want to maximize the torque to get the best performance. Therefore, the angle between the rotor magnetic field and stator magnetic field should be controlled to be orthogonal in order to produce the maximum torque and the best electromechanical conversion. The rotating magnetic field generated from the stator windings is the key that we need to control, by controlling the stator currents. The rotor's instant position needs to be tracked in order to adjust the position of the stator magnetic field and ensure a maximum generated torque. In addition, we tune up the parameters in the PID compensator and implement the closed loop control. By doing that, we can achieve a good control with a minimum amount of current input drawn [105] - [118].

In this chapter, we design the drive system and implement the field oriented control algorithm into the micro-controller. Besides, we successfully drive the designed motor by the sensorless motor controller.

The rest of the chapter is organized as follows. The dynamic modeling of the PMSM is presented in section 4.2. The space vector PWM control principles are introduced in section 4.3. The fundamental principle of FOC is presented in section 4.4. Thermal considerations are discussed in section 4.5. We implement the control algorithm and build a controller prototype in section 4.6. Section 4.7 introduces an updated inverter design targeting for higher power applications. Finally, we conclude the chapter in section 4.8.

4.2 Dynamic Modeling

It is complicated when doing the analysis directly on a three-phase reference frame of the stator. Instead, when people start to transform the three-phase abc quantities into two constant d-q quantities, calculations become a lot easier. The transformation is called $dq0$ transformation. As described earlier, the magnetic torque is created by the interaction of the rotor magnetic field generated either from the permanent magnet or electromagnet and the induced magnetic field from the stator windings. A maximum value of the torque occurs when the rotor magnetic field is orthogonal to the stator magnetic field. In another word, we can get the maximized torque if we can control the stator winding current to generate a field which is orthogonal to the rotor magnetic field. The new reference frame called $dq0$ frame will give us a help to do the analysis. We align the stator flux with the q axis of the rotor flux, as shown in Fig. 4.1. Furthermore, the stator current component on q axis is controlled to generate the commanded torque, and the component on d axis is set to zero.

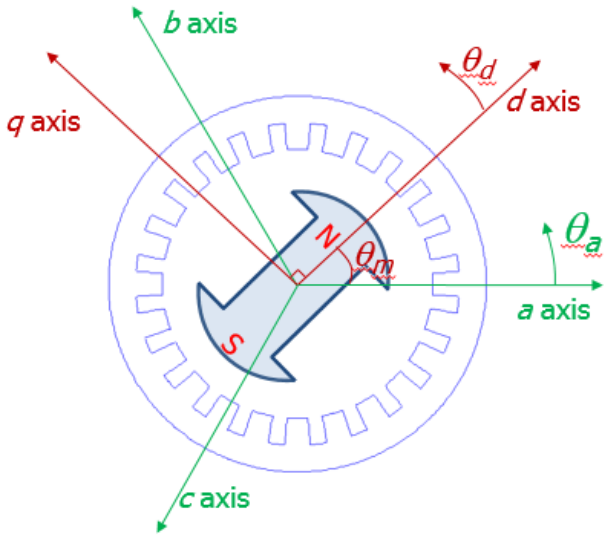

Figure 4.1: d-q axis on synchronous machine.

We will need to jump out of the rotating reference frame back to the stationary coordinate system to make the modulated correction voltages onto motor terminals through Reverse Park's and Reverse Clarke's Transformations.

It is possible that the motor needs to be controlled under such circumstances as frequently ramp up or down. Therefore, the control design has to consider the dynamic behavior of the motor. The transformation for a PM motor is described by the following equation:

$$\mathbf{S}_{dq0} = \mathbf{K}\mathbf{S}_{abc}, \tag{4.1}$$

and its inverse format is

$$\mathbf{S}_{abc} = \mathbf{K}^{-1}\mathbf{S}_{dq0}, \tag{4.2}$$

where S can represent the variables such as voltage (V), current (i), or flux linkage (λ), etc. In addition, $\mathbf{K}$ matrix and its inverse format can be seen in Eqn. 4.3:

$$\mathbf{K} = \frac{2}{3}\begin{bmatrix} cos(\theta_{me}) & cos(\theta_{me} - 2\pi/3) & cos(\theta_{me} + 2\pi/3) \\ -sin(\theta_{me}) & -sin(\theta_{me} - 2\pi/3) & -sin(\theta_{me} + 2\pi/3) \\ 1/2 & 1/2 & 1/2 \end{bmatrix}$$

$$\mathbf{K}^{-1} = \begin{bmatrix} cos(\theta_{me}) & -sin(\theta_{me}) & 1 \\ cos(\theta_{me} - 2\pi/3) & -sin(\theta_{me} - 2\pi/3) & 1 \\ cos(\theta_{me} + 2\pi/3) & -sin(\theta_{me} + 2\pi/3) & 1 \end{bmatrix}, \tag{4.3}$$

where

$$\theta_{me} = \frac{p}{2}\theta_m, \tag{4.4}$$

where p represents the number of poles, and θ_m is the rotor rotational angle. By using the $\mathbf{K}$ matrix

transformation, we can transform the abc reference frame to d-q reference frame, vice versa.

Originally, the stator winding voltages on the abc reference frame can be presented by

$$\mathbf{V}_{abc} = \mathbf{R}_s \mathbf{i}_{abc} + \frac{d}{dt}\boldsymbol{\lambda}_{abc}, \tag{4.5}$$

which represents the phase voltage expression as a function of the phase resistance, current, and flux linkage.

For rotor who uses field winding on it and with damper winding, the final expression of the voltage on both the stator and rotor after applying the $\mathbf{K}$ matrix is:

$$\begin{bmatrix} V_d \\ V_q \\ V_0 \\ V_f \\ 0 \\ 0 \end{bmatrix} = \begin{bmatrix} R_s i_d + \frac{d}{dt}\lambda_d - \lambda_q \omega_{me} \\ R_s i_q + \frac{d}{dt}\lambda_q + \lambda_d \omega_{me} \\ R_s i_0 + \frac{d}{dt}\lambda_0 \\ R_f i_f + \frac{d}{dt}\lambda_f \\ R_{k_d} i_{k_d} + \frac{d}{dt}\lambda_{k_d} \\ R_{k_q} i_{k_q} + \frac{d}{dt}\lambda_{k_q} \end{bmatrix}. \tag{4.6}$$

In order to model the flux linkage, we need to relate the current to it by the inductance. For a salient pole rotor structure, the inductance can be generally expressed as the equation in the following [119] [120].

$$\mathbf{L}_{abcf} = \begin{bmatrix} \mathbf{L}_{ss} & \mathbf{L}_{sr} \\ \mathbf{L}_{sr}^T & \mathbf{L}_{rr} \end{bmatrix}, \tag{4.7}$$

where

$$\mathbf{L}_{ss} = \begin{bmatrix} L_{aa} & L_{ab} & L_{ac} \\ L_{ba} & L_{bb} & L_{bc} \\ L_{ca} & L_{cb} & L_{cc} \end{bmatrix}, \tag{4.8}$$

$$\mathbf{L}_{sr} = \begin{bmatrix} L_{af} & L_{ak_d} & L_{ak_q} \\ L_{bf} & L_{bk_d} & L_{bk_q} \\ L_{cf} & L_{ck_d} & L_{ck_q} \end{bmatrix}, \tag{4.9}$$

and

$$\mathbf{L}_{rr} = \begin{bmatrix} L_{f} & L_{fk_d} & L_{fk_q} \\ L_{k_df} & L_{k_d} & L_{k_dk_q} \\ L_{k_qf} & L_{k_qk_d} & L_{k_q} \end{bmatrix}. \tag{4.10}$$

The terms in Eqn. 4.8 can be substituted by

$$\begin{cases} L_{aa} = L_{ls} + L_A + L_B cos2\theta_{me} \\ L_{bb} = L_{ls} + L_A + L_B cos2(\theta_{me} - \frac{2\pi}{3}) \\ L_{cc} = L_{ls} + L_A + L_B cos2(\theta_{me} + \frac{2\pi}{3}) \\ L_{ab} = L_{ba} = -\frac{1}{2}L_A + L_B cos(2\theta_{me} - \frac{2\pi}{3}) \\ L_{bc} = L_{cb} = -\frac{1}{2}L_A + L_B cos(2\theta_{me}) \\ L_{ac} = L_{ca} = -\frac{1}{2}L_A + L_B cos(2\theta_{me} + \frac{2\pi}{3}). \end{cases} \tag{4.11}$$

The terms in Eqn. 4.9 can be substituted by

$$\begin{cases} L_{af} = L_{fa} = L_{sf}cos(\theta_{me}) \\ L_{bf} = L_{fb} = L_{sf}cos(\theta_{me} - \frac{2\pi}{3}) \\ L_{cf} = L_{fc} = L_{sf}cos(\theta_{me} + \frac{2\pi}{3}) \\ L_{ak_d} = L_{k_da} = L_{sk_d}cos(\theta_{me}) \\ L_{bk_d} = L_{k_db} = L_{sk_d}cos(\theta_{me} - \frac{2\pi}{3}) \\ L_{ck_d} = L_{k_dc} = -L_{sk_d}cos(\theta_{me} + \frac{2\pi}{3}) \\ L_{ak_q} = L_{k_qa} = -L_{sk_q}sin(\theta_{me}) \\ L_{bk_q} = L_{k_qb} = -L_{sk_q}sin(\theta_{me} - \frac{2\pi}{3}) \\ L_{ck_q} = L_{k_qc} = -L_{sk_q}sin(\theta_{me} + \frac{2\pi}{3}). \end{cases} \tag{4.12}$$

The terms in Eqn. 4.10 can be substituted by

$$\begin{cases} L_f = L_{lf} + L_{mf} \\ L_{k_d} = L_{lk_d} + L_{mk_d} \\ L_{k_q} = L_{lk_q} + L_{mk_q} \\ L_{fk_d} = L_{k_df} \\ L_{fk_q} = L_{k_qf} = 0 \\ L_{k_dk_q} = L_{k_qk_d} = 0. \end{cases} \tag{4.13}$$

Until now, we have the derivations of the inductance matrix in abc frame. In addition, we can get the matrix in a d-q frame and further get the flux linkage matrix linked with the current.

$$\boldsymbol{\lambda}_{abcf} = \mathbf{L}_{abcf}\mathbf{i}_{abcf}. \tag{4.14}$$

Then we can have the flux linkage in a matrix expression for conciseness:

$$\mathbf{L}_{dqf} = \begin{bmatrix} L_d & 0 & 0 & L_{sf} & L_{sk_d} & 0 \\ 0 & L_q & 0 & 0 & 0 & L_{sk_q} \\ 0 & 0 & L_0 & 0 & 0 & 0 \\ \frac{3}{2}L_{sf} & 0 & 0 & L_f & L_{fk_d} & 0 \\ \frac{3}{2}L_{sk_d} & 0 & 0 & L_{k_df} & L_{k_d} & 0 \\ 0 & \frac{3}{2}L_{sk_q} & 0 & 0 & 0 & L_{k_q}. \end{bmatrix}, \tag{4.15}$$

where

$$\begin{cases} L_d = L_{ls} + L_{md} \\ L_q = L_{ls} + L_{mq} \\ L_{ls} = L_0 \end{cases}, \tag{4.16}$$

and

$$\begin{cases} L_{md} = \frac{3}{2}(L_A + L_B) \\ L_{mq} = \frac{3}{2}(L_A - L_B). \end{cases} \tag{4.17}$$

The instantaneous input power on the stator windings can also be expressed through $dq0$ theory:

$$P_{in} = \frac{3}{2}R_s(i_d^2 + i_q^2 + 2i_0^2) + \frac{3}{2}(i_d\frac{d\lambda_d}{dt} + i_q\frac{d\lambda_q}{dt} + 2i_0\frac{d\lambda_0}{dt}) + \frac{3}{2}\frac{P}{2}\omega_m(\lambda_d i_q - \lambda_q i_d). \tag{4.18}$$

The third term of the equation above is the mechanical power. Thus, we can get the expression of the electromagnetic torque on the rotor

$$T_e = \frac{P_{mech}}{\omega_m} = \frac{3}{2}\frac{P}{2}(\lambda_d i_q - \lambda_q i_d). \tag{4.19}$$

For the rotor without a damper winding, the analysis would be easier. The voltages on the stator and rotor can be expressed in a matrix format as

$$\begin{bmatrix} V_d \\ V_q \\ V_0 \\ V_f \end{bmatrix} = \begin{bmatrix} R_s i_d + \frac{d}{dt}\lambda_d - \lambda_q \omega_{me} \\ R_s i_q + \frac{d}{dt}\lambda_q + \lambda_d \omega_{me} \\ R_s i_0 + \frac{d}{dt}\lambda_0 \\ R_f i_f + \frac{d}{dt}\lambda_f \end{bmatrix}. \tag{4.20}$$

The inductance matrix on abc frame should be

$$\mathbf{L}_{abcf} = \begin{bmatrix} \mathbf{L}_{ss} & \mathbf{L}_{sf} \\ \mathbf{L}_{sf}^T & \mathbf{L}_f \end{bmatrix}, \tag{4.21}$$

where

$$\mathbf{L}_{sf} = \begin{bmatrix} \mathbf{L}_{af} \\ \mathbf{L}_{bf} \\ \mathbf{L}_{cf} \end{bmatrix}. \tag{4.22}$$

The flux linkage expression becomes

$$\boldsymbol{\lambda}_{abcf} = \begin{bmatrix} \boldsymbol{\lambda}_{abc} \\ \boldsymbol{\lambda}_f \end{bmatrix}. \tag{4.23}$$

The current expression becomes

$$\mathbf{i}_{abcf} = \begin{bmatrix} \mathbf{i}_{abc} \\ i_f \end{bmatrix}. \tag{4.24}$$

Winding flux linkage on the stator after being converted to d-q frame is

$$\boldsymbol{\lambda}_{dq0} = (\mathbf{K}\mathbf{L}_{ss}\mathbf{K}^{-1})\mathbf{i}_{dq0} + \mathbf{K}\mathbf{L}_{sf}i_f. \tag{4.25}$$

Besides, from Eqn. 4.21, we have $\mathbf{L}_{dqf}$:

$$\mathbf{L}_{dqf} = \begin{bmatrix} \mathbf{K}\mathbf{L}_{ss}\mathbf{K}^{-1} & \mathbf{K}\mathbf{L}_{sf} \\ \mathbf{L}_{sf}^{T}\mathbf{K}^{-1} & L_f \end{bmatrix}. \tag{4.26}$$

With windings replaced by the permanent magnet on the rotor, the dynamical modeling is actually a lot easier to be analyzed. Fig. 4.2 shows a structure of a two-pole permanent magnet machine.

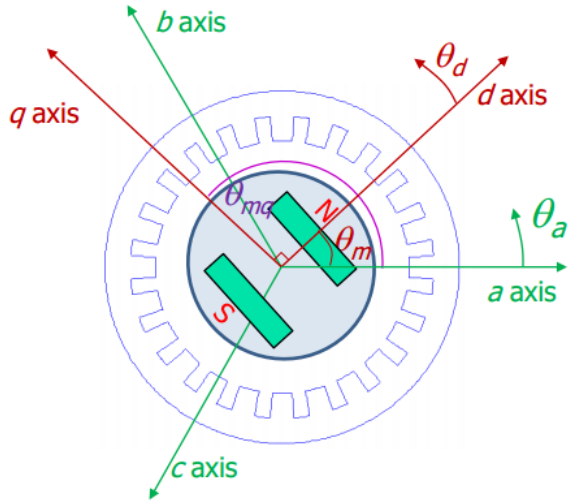

Figure 4.2: d-q axis on permanent magnet machine.

The derivations would be very similar with the previous type of machine with the field winding on the rotor. Instead, the flux linkage on the rotor will only come from the permanent magnet, λ_{PM}. The final expressions are presented in the following. The detail derivation is skipped. The flux linkage on the abc frame is

$$\boldsymbol{\lambda}_{abc} = \mathbf{L}_{abc}\mathbf{i}_{abc} + \boldsymbol{\lambda}_{PMabc}. \tag{4.27}$$

and its expression on d-q frame is

$$\boldsymbol{\lambda}_{dq0} = \mathbf{L}_{dq0}\mathbf{i}_{dq0} + \boldsymbol{\lambda}_{PMdq0}. \tag{4.28}$$

The voltage on d-q frame will be

$$\mathbf{V} = \begin{bmatrix} V_d - R_s i_d + \lambda_q \omega_{me} \\ V_q - R_s i_q - \lambda_d \omega_{me} \\ V_0 - R_s i_0 \end{bmatrix}, \tag{4.29}$$

where

$$\lambda_d = L_d i_d + \lambda_{PM}, \tag{4.30}$$

$$\lambda_q = L_q i_q. \tag{4.31}$$

And, the electromagnetic torque on a PM machine is

$$T_e = \frac{P_{mech}}{\omega_m} = \frac{3}{2}\frac{P}{2}[\lambda_{PM} i_q + (L_d - L_q) i_d i_q]. \tag{4.32}$$

For round rotor PM machine, the inductance on d and q should be equal. Thus, the EM torque will only be a function of the q axis current i_q only since λ_{PM} is constant. It would be a lot easier to control one variable in order to control the torque.

We can apply the dynamic equations to describe the motor's non-linear behavior. There are primary four equations that decide the dynamical characteristics of the motor from Eqn. 4.33 to Eqn. 4.36.

$$\frac{di_d}{dt} = \frac{1}{L_d}(-R_s i_d + p/2\omega_m L_q i_q + u_d) \tag{4.33}$$

$$\frac{di_q}{dt} = \frac{1}{L_q}(-R_s i_q - p/2\omega_m L_d i_d - p/2\omega_m \lambda_{PM} + u_q) \tag{4.34}$$

$$\frac{d\omega_m}{dt} = \frac{1}{J}(T_e - T_L - c\omega_m) \tag{4.35}$$

$$\frac{d\theta_m}{dt} = \omega_m, \tag{4.36}$$

where u_d describes the input voltage on d axis, u_q represents the input voltage on q axis, T_L is the load torque, J is the moment of inertia of the rotor, and c represents a coefficient of friction.

A block diagram can illustrate the transformation model in Fig. 4.3, which explains that the three-phase abc voltages can be converted to d-q system, then fed into the dynamical equations, the output can be converted back to abc reference frame, and fed back to the motor terminals. In addition, the motor's dynamical model by simulink is shown in Fig. 4.4. It shows the transformation between abc and $dq0$ reference frame as well as the feedback to the dynamical equations.

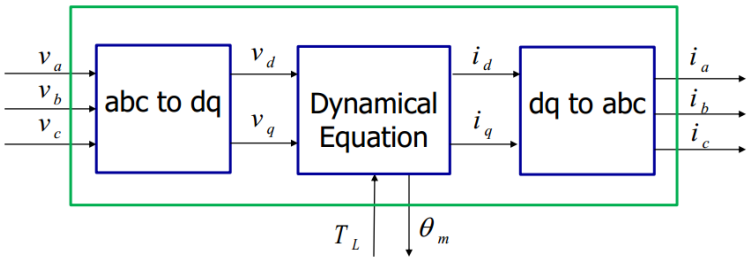

Figure 4.3: Transformation model.

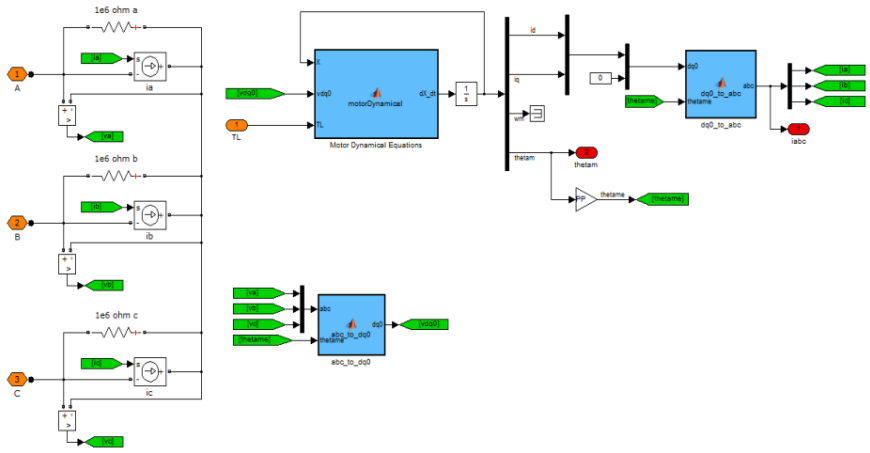

Figure 4.4: Dynamic model of the motor.

4.3 Space Vector Modulation

The three-phase inverter made of MOSFET bridges and Y-connection load can be described as shown in Fig. 4.5. There are eight different states including two redundant vectors and six other active vectors with different switches from S_1 to S_6. It is good to be pointed out that S_1 and S_2 are always complementary, so do S_3 and S_4, S_5 and S_6 [121].

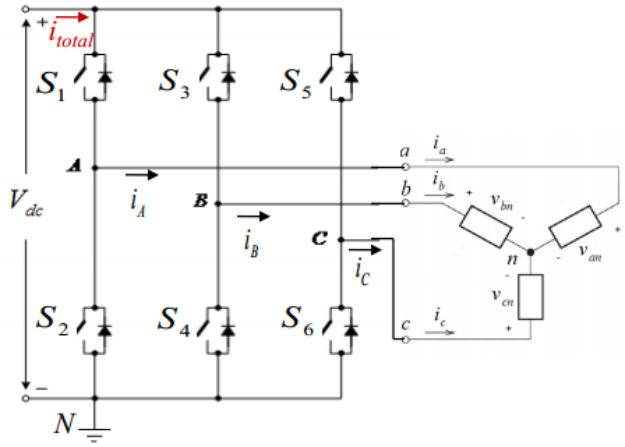

Figure 4.5: Three-phase circuit.

In the space vector PWM (SVPWM) modulation, with the switch of the MOSFET and a desired duty cycle in each phase, it comes up to various combinations as shown in Table. 4.1. The space vector representation can be expressed as

$$\overrightarrow{V}(t) = \frac{2}{3}[V_{An}(t)e^{j0} + V_{Bn}(t)e^{j2\pi/3} + V_{Cn}(t)e^{j4\pi/3}]. \tag{4.37}$$

Accordingly, a space vector diagram that can show the space vector representation is in Fig. 4.6. Valid states are from V_1 to V_6 [121].

Table 4.1: Switching states.

Space Vector		Switching State (Three Phases)	On-state Switch	Vector Definition
Zero Vector	$\vec{V}_0$	[111]	S_1, S_3, S_5	$\vec{V}_0 = 0$
		[000]	S_2, S_4, S_6	
Active Vector	$\vec{V}_1$	[100]	S_1, S_4, S_6	$\vec{V}_1 = \frac{2}{3} V_d e^{j0}$
	$\vec{V}_2$	[110]	S_1, S_3, S_6	$\vec{V}_2 = \frac{2}{3} V_d e^{j\frac{\pi}{3}}$
	$\vec{V}_3$	[010]	S_2, S_3, S_6	$\vec{V}_3 = \frac{2}{3} V_d e^{j\frac{2\pi}{3}}$
	$\vec{V}_4$	[011]	S_2, S_3, S_5	$\vec{V}_4 = \frac{2}{3} V_d e^{j\frac{3\pi}{3}}$
	$\vec{V}_5$	[001]	S_2, S_4, S_5	$\vec{V}_5 = \frac{2}{3} V_d e^{j\frac{4\pi}{3}}$
	$\vec{V}_6$	[101]	S_1, S_4, S_5	$\vec{V}_6 = \frac{2}{3} V_d e^{j\frac{5\pi}{3}}$

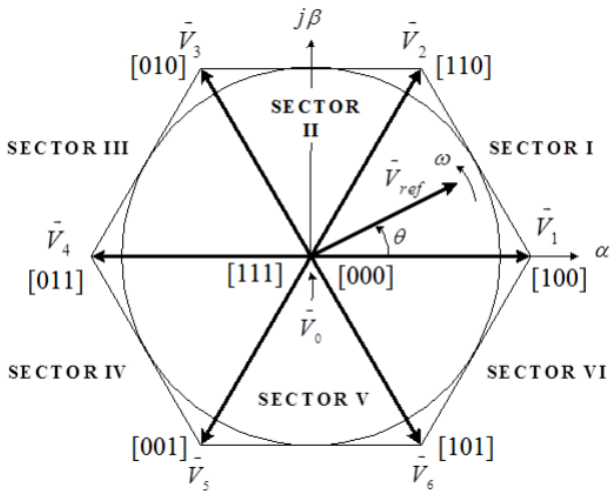

Figure 4.6: Space vector diagram.

We can have a general expression for the space vector, which is

$$\overrightarrow{V}_k = \frac{2}{3} V_d e^{j(k-1)\frac{\pi}{3}}, \tag{4.38}$$

where k= 1,2,...,6, and V_d is the dc bus voltage.

Generally speaking, SVPWM method generates less harmonic distortion in the output voltages or currents in comparison with the sinusoidal PWM method. Besides, SVPWM utilizes the source voltage more efficiently compared to the sinusoidal PWM.

4.4 Field Oriented Control System

The Field Oriented Control (FOC) is an adaptive and closed loop process which can iteratively update the current and speed value through a PID compensator. The key of FOC is to decouple the torque and magnetization flux component of the winding current in the PMSM. In addition to that, a good control algorithm can be applied so that it can achieve better dynamic performance.

The controller provides the closed loop feedback to the input of the system. It will record the rotor position and calculate the required amount of voltage input to the motor terminals, and then send gate control signals to the MOSFETs. A block diagram of the controller is shown in Fig. 4.7. We describe it as three main control loops: current loop, speed loop and position loop. In each of these loops, a PI controller is applied to tune up the subsystem in order to minimize the error signal [122]. A DSP based micro-controller is used to assure a fast mathematical processing.

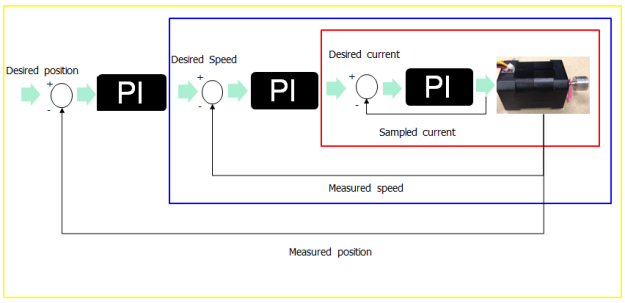

Figure 4.7: Closed loop control.

Two motor phase currents i_a, i_b are sampled as shown in Fig. 4.8. These measurements go to the Clarke's Transformation module. The outputs coming out of this module are i_α and i_β. Next, these two components of the currents are the inputs of the Park's Transformation module which generates i_d, i_q. These two current components on d-q frame are compared to the reference i_{dref} and i_{qref} through a PI controller. After the comparison, the modulated voltages, V_d and V_q, become the inputs of the inverse Park's Transformation module. The outputs of this are V_α and V_β. They will be applied to the space vector PWM module. The output PWM signals will drive the inverter.

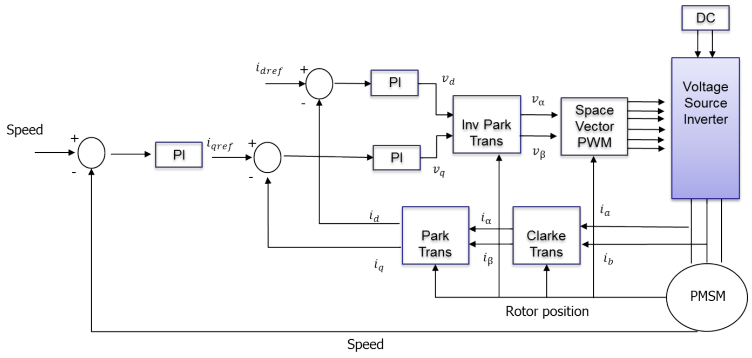

Figure 4.8: Control scheme of FOC.

Rotor angle is an important parameter in the FOC control. A position sensor in the market not only increases the cost, maintenance work and complexity, but also causes problems to the system robustness and reliability. Thus, sensorless control method is valuable to our design [123] - [129]. In FOC, the rotor angle is estimated by a sliding mode observer (SMO). The SMO module contains a first order low-pass filter for the back-EMF estimation. However, the low pass filter will cause a delay in the estimated angle. In order to accurately achieve the FOC algorithm, compensation is made to the estimated angle. The phase lag differs at various speeds, and therefore, the compensation must be adaptive. The angle delay is calibrated at different speeds utilizing a function to interpolate the delay angle vs. speed curve. The appropriate phase lag compensation is automatically calculated based on the speed of the motor and applied to the feedback loop. This adaptive phase lag compensation increases the accuracy of the control.

It is required and desirable to produce the rated power with the highest attainable speed for many applications such as electric vehicles. However, due to the upper limit placed on the dc bus voltage and current ratings of a given inverter, the motor's input voltage and current ratings are limited as well. In addition, the limit of the voltage and current impacts the maximum speed with the rated torque and the maximum torque generation of the motor drive system, respectively. For example, above certain speed, the induced voltage in the winding would exceed the maximum input voltage, making the flow of the current back into the machine terminals. In order to solve the problem, the induced voltage has to be constrained to be less than the applied voltage by weakening the air gap flux linkages, which is by adding a negative d axis current to compensate for the increasing of the induced voltage [122].

4.5 Thermal Analysis

The temperature rise with the actual power consumption by the device is related to the thermal resistance. The simulation of temperature distribution is more accurate than the analytical calculation. We build a simple thermal model with the MOSFETs and a fan as we can see in Fig. 4.9. Since the power dissipated as heat will be primarily on the MOSFETs, it will be minor losses on the other components of the inverter. Therefore, we ignore them in the thermal model to reduce the complicity of the simulation [130] - [137].

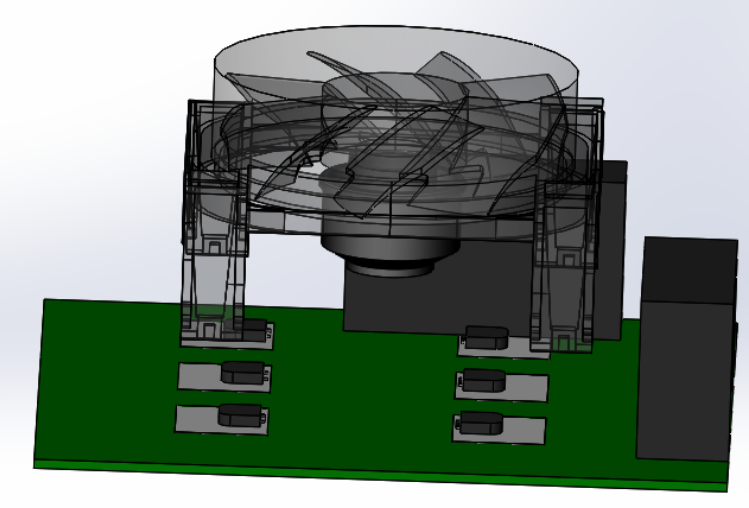

Figure 4.9: Simplified thermal modeling of the controller.

Fig. 4.10 shows the temperature distribution, from which we can see the hot spot of the system. Therefore, as long as we can keep the worst-case scenario, which is the temperature of the most hot spot, under the control, we can assure the whole system will work. In addition, the simulation can also help to choose a fan with the proper air flow value in cubic feet per minute (CFM).

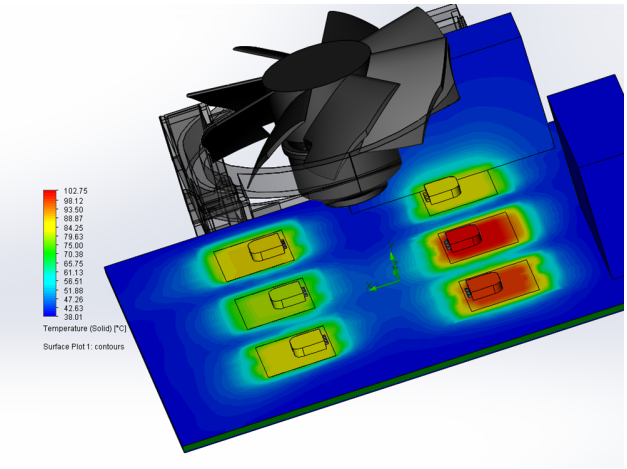

Figure 4.10: Temperature distribution.

4.6 Inverter Prototype and Test

We apply the FOC principle into the micro-controller to achieve the control system design. Based on that, we have designed the inverter system and built the controller prototype as shown in Fig. 4.11. Current sensors are being applied to sample the terminal phase currents. Besides, we try to avoid the signal disturbances by separating the trace routing of the small signals from the bus power.

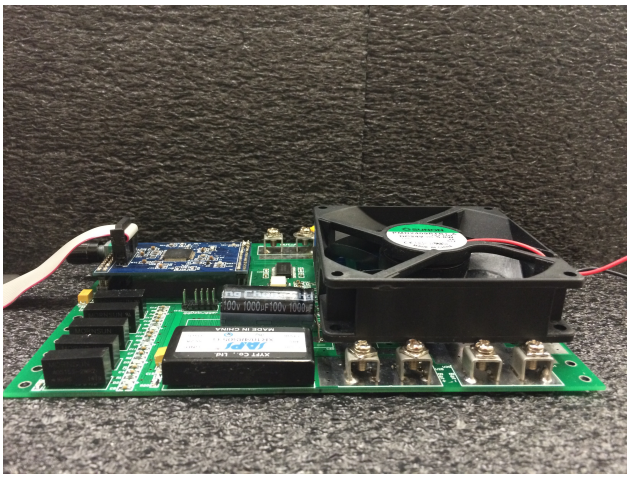

Figure 4.11: Three-phase DC to AC inverter.

As shown in Fig. 4.12, we use a motor-generator pair with electric load to build the test system. DC power from a battery set is fed into the DC to AC inverter to power the motor using the controller, which in turn drives the generator, the power coming out of the generator is dissipated by a resistor bank. We can adjust the power output by changing the rotational speed of the rotor. The inverter is designed for up to 2 kW equipped with a cooling fan.

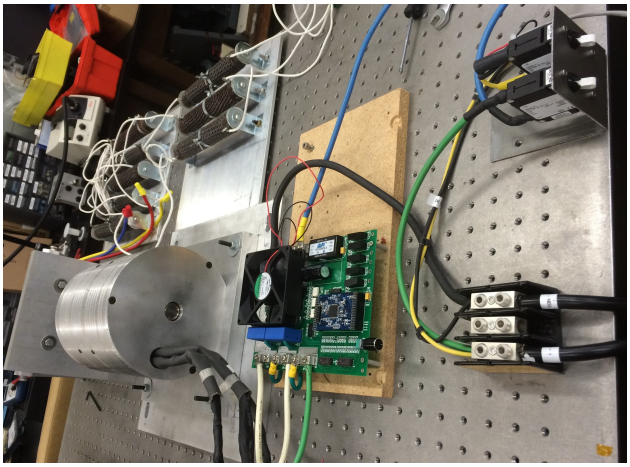

Figure 4.12: System test.

Since we have implemented the sensorless control rather than a position sensor, the SMO is responsible for recording the position of the rotor. After a transient time, which is a very short initial start up period when the initial position of the rotor is detected, the SMO algorithm captures the position of the stator magnetic field and send signals to the motor phase terminals. The sampled phase current is compared to the commanded current. The estimation of the back-EMF is not correct according to the non-linear variation of the motor's parameters if there is an error signal existing between the sampled current and commanded current. Thus, the algorithm will automatically re-estimate the back-EMF value until the sampled current matches the commanded value. In another word, the error signal between them will eventually converge to zero. In Fig. 4.13, the blue curve shows that the SMO can successful record the movement of the rotor in the range of 0 to 2π.

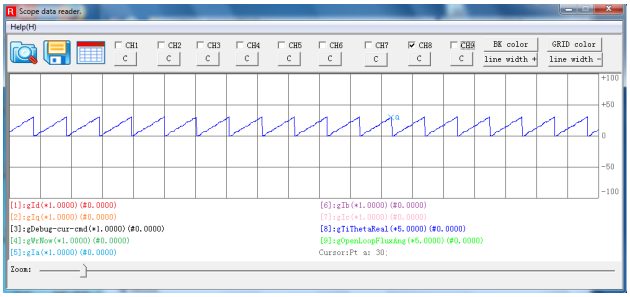

Figure 4.13: Position measurement.

At the initial start up, the machine needs a large start up I_d current to generate enough start up torque. The software needs to capture the initial position of the rotor before the algorithm begins. By applying a large current, the rotor will quickly be attracted to a nearest position due to the interaction of the electromagnet and permanent magnet. Firstly, verification of the currents on both d and q axis can be controlled as we need is necessary as shown in Fig. 4.14. The red line represents the commanded value we give to the software, and the green curve follows the red line. The blue curve is set to be zero.

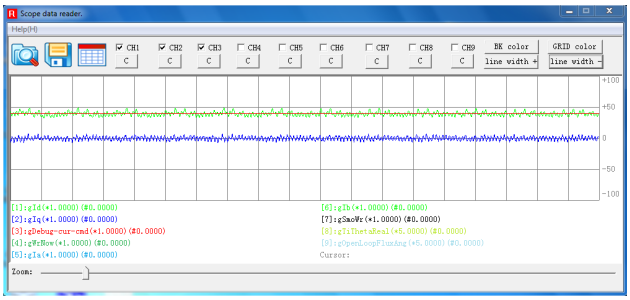

Figure 4.14: d-q currents follow the commanded value.

Secondly, as shown in Fig. 4.15, the red curve represents I_d, which starts from zero, reaches up to about 70 amps for a short period, then drops down to zero. I_q begins to rise right after I_d

is down to zero. The blue curve stands for the mechanical speed of the rotor, which shows it will begin to speed up smoothly after the initial transient time period. Besides, Fig. 4.16 shows the currents of I_a and I_b at the initial start up.

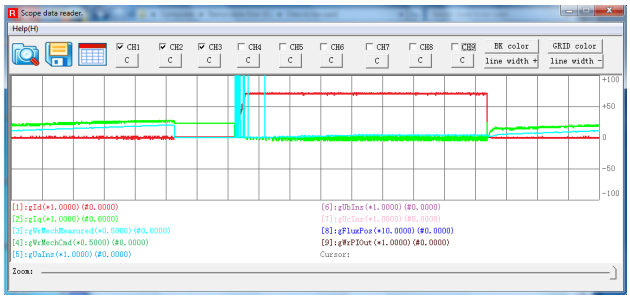

Figure 4.15: d-q currents and rotating speed at the initial start up.

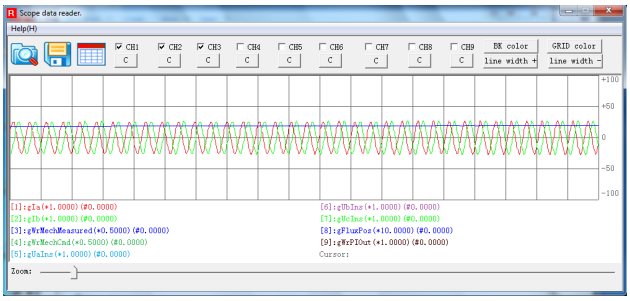

Figure 4.16: I_a, I_b currents and rotating speed at the initial start up.

The full load operation is achieved when the machine is running at 2000 rpm. Besides, we have also recorded the performance of the system running at 500 rpm, 1000 rpm and 1500 rpm. It is necessary to test and prove that the system can have a reliable operation at various loads.

At 500 rpm, I_q is about 29 amps, and I_d current is zero as in Fig. 4.17. I_q is controlled to generate the torque component. The I_a and I_b currents are shown in Fig. 4.18.

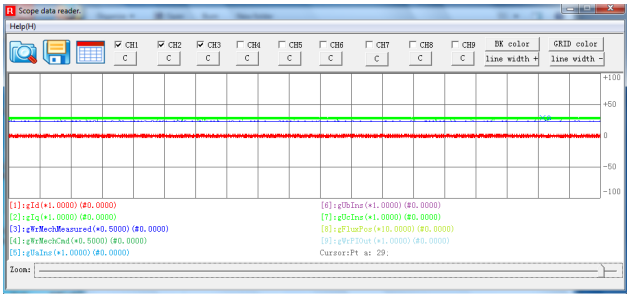

Figure 4.17: d-q currents and rotating speed at 500 rpm.

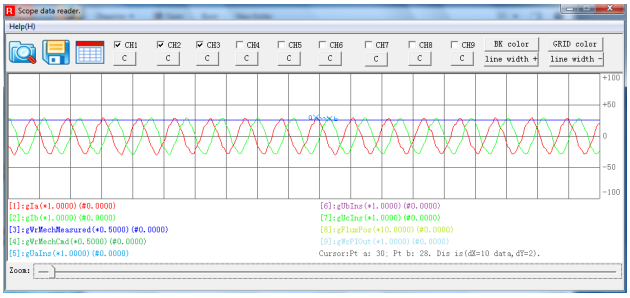

Figure 4.18: Phase currents and rotating speed at 500 rpm.

Moreover, terminal voltages U_a, U_b and U_c are shown in Fig. 4.19. They are curves similar with sinusoidal distribution. We capture them in the test software created by Visual C++.

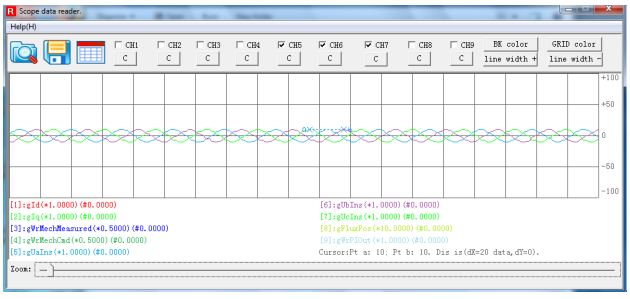

Figure 4.19: Phase voltages at 500 rpm.

As the speed increases to 1000 rpm, I_q turns out to be about 37 amps, and I_d current is zero as in Fig. 4.20. And, the new I_a and I_b currents are shown in Fig. 4.21.

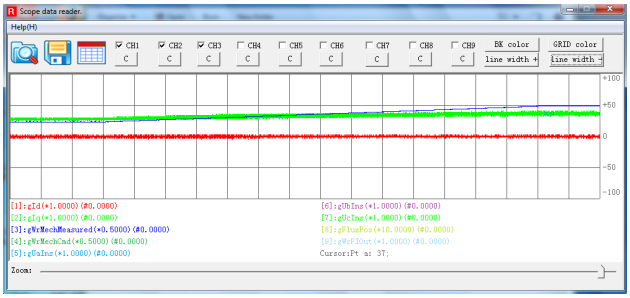

Figure 4.20: d-q currents and rotating speed at 1000 rpm.

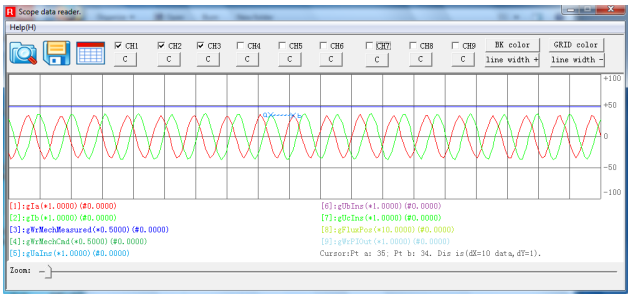

Figure 4.21: Phase currents and rotating speed at 1000 rpm.

Terminal voltages of U_a, U_b and U_c are shown in Fig. 4.22 with the machine running at 1000 rpm.

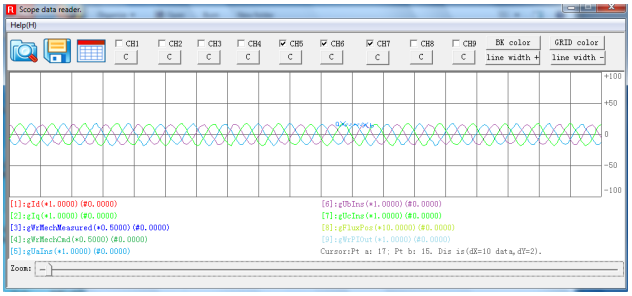

Figure 4.22: Phase voltages at 1000 rpm.

The screen shot result captured from the oscilloscope shown as PWM output of the line-to-line voltages when the machine is running at 1000 rpm is presented in Fig. 4.23.

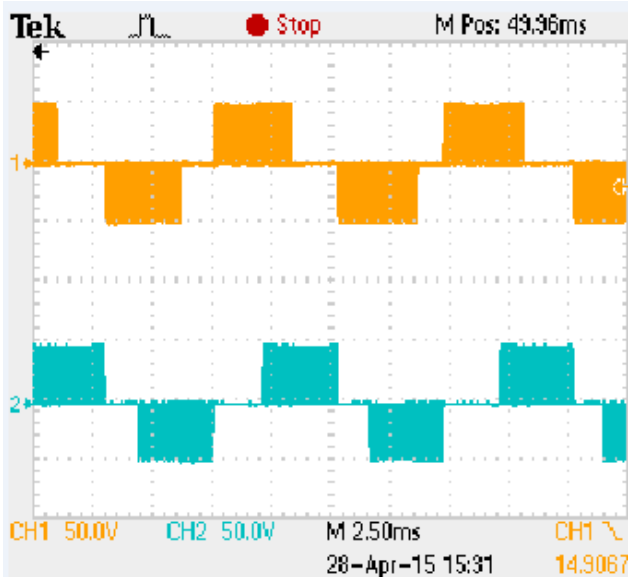

Figure 4.23: PWM output of the line to line voltages at 1000 rpm.

Once the speed reaches 1500 rpm, I_q and I_d current are illustrated in Fig. 4.24. The I_a and I_b currents are shown in Fig. 4.25. We can see the current variation as the speed increases.

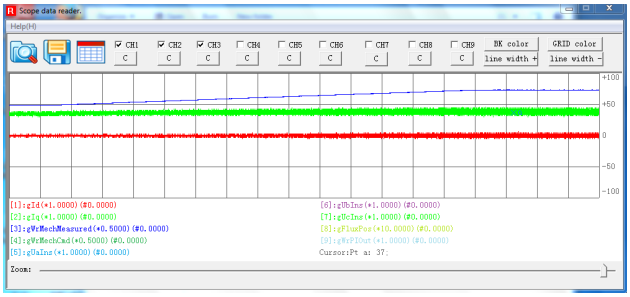

Figure 4.24: d-q currents and rotating speed at 1500 rpm.

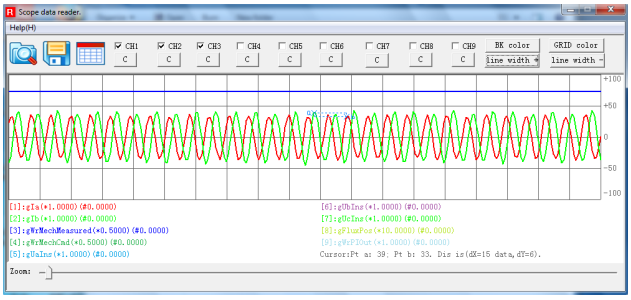

Figure 4.25: Phase currents and rotating speed at 1500 rpm.

Similarly, the terminal voltages of U_a, U_b and U_c are shown in Fig. 4.26 with larger peak to peak values.

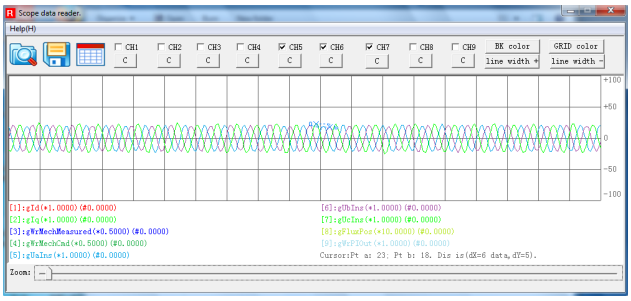

Figure 4.26: Phase voltages at 1500 rpm.

The screen shot result captured from the oscilloscope shown as the PWM output of the line-to-line voltages when the machine is running at 1500 rpm is presented in Fig. 4.27.

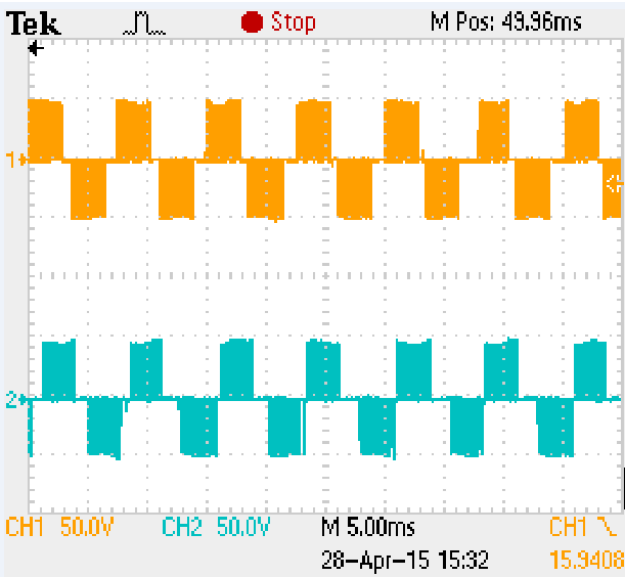

Figure 4.27: PWM output of the line to line voltages at 1500 rpm.

As the speed reaches up to 2000 rpm, I_d current is zero as it supposed to be, while I_q is constant at around 40 amps, which is illustrated in Fig. 4.28. The I_a and I_b currents are also shown in Fig. 4.29.

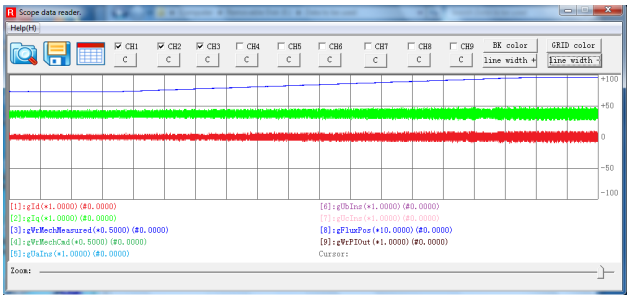

Figure 4.28: d-q currents and rotating speed at 2000 rpm.

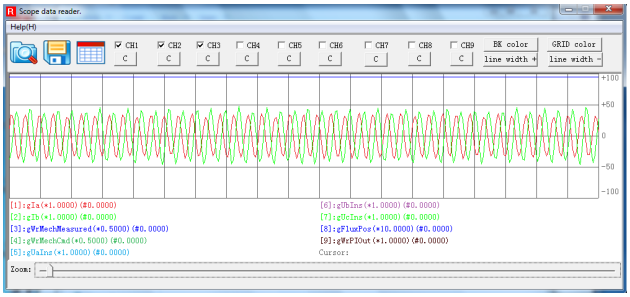

Figure 4.29: Phase currents and rotating speed at 2000 rpm.

Terminal voltages of U_a, U_b and U_c are shown in Fig. 4.30. The screen shot result captured from the oscilloscope shown as the PWM output of the line-to-line voltages when the machine is running at 2000 rpm is presented in Fig. 4.31. We can confirm the mechanical speed of the machine by measuring the electrical frequency of the PWM waveform.

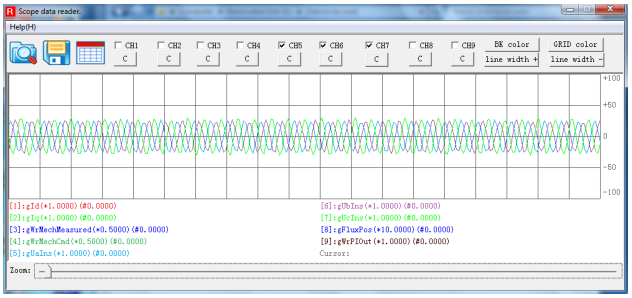

Figure 4.30: Phase voltages at 2000 rpm.

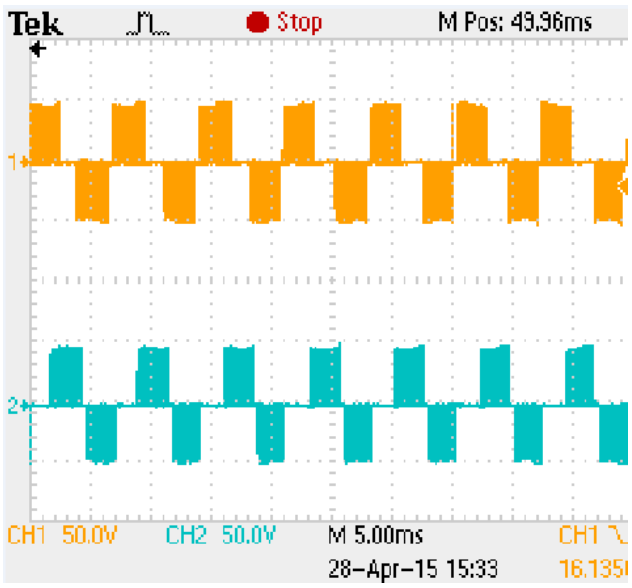

Figure 4.31: PWM output of the line to line voltages at 2000 rpm.

4.7 High Power Applications

As shown in Fig. 4.11, for the current inverter topology, we have to use a fan to dissipate the heat generated. There is limited room for attaching a powerful heat sink. However, for further optimization, we have researched on building new structure with an aluminum board for the high power transfer, the updated design is shown in Fig. 4.32. The bus power traces have been placed on the aluminum board and we have the option to further attach it to additional metal plate in order to increase the thermal management capability. Copper bar is very powerful in carrying large current. We therefore use the copper bars for the bus power. The inverter would be able to deliver higher power even up to 5 kW without the need for a cooling fan and the overall size of the control board is reduced by about 40%.

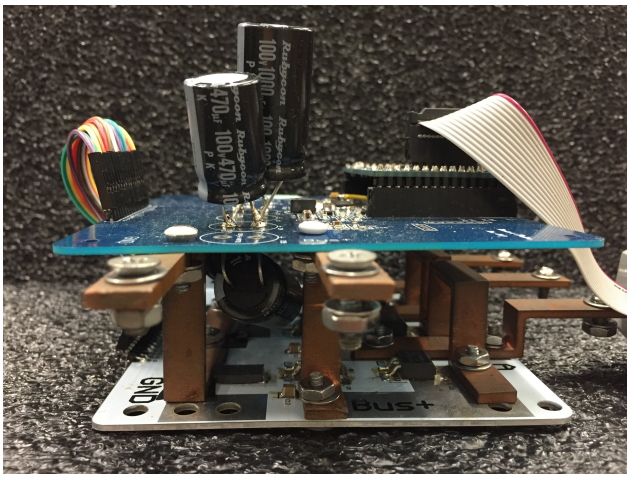

Figure 4.32: Inverter design by using aluminum board.

4.8 Summary

We have introduced the fundamental $dq0$ control theory of the PM motor. We presented the derivations, including voltages, inductances, flux linkages, etc. and the motor dynamic modeling. We discussed the space vector PWM. In addition, FOC principle and the control methodology for the motor control system have been introduced. According to that, an inverter topology has been proposed and the PCB layout has been completed. Thermal issues of the PCB board are considered through computational fluid dynamics (CFD) simulation. We built a prototype of the designed controller and have tested with the designed motor as a complete system. The test results are provided. Furthermore, we optimized the inverter topology which can completely avoid the need for a cooling fan by applying an aluminum board structure for the bus power design.

CHAPTER 5: DESIGN OF A PERMANENT MAGNET SYNCHRONOUS MOTOR WITH WIDE TEMPERATURE RANGE

5.1 Introduction

Super compact permanent magnet synchronous motors with wide temperature range are in great demand for industrial applications such as mineral mining, aerospace engineering, defense applications, etc. These applications usually occur in either extremely cold or hot environment. The performance of the magnetic materials depends highly on the operating temperature. Many materials are subject to degradation of performance with an increase in temperature. Although NdFeB is the strongest permanent magnet, it can only operate at an ambient temperature up to $150\,^{\circ}$C. SmCo is the second strongest permanent magnet, which can operate from cryogenic temperature up to $350\,^{\circ}$C. Therefore, we will choose SmCo as the permanent magnet material. Soft magnetic materials such as steels usually saturate at magnetic flux density around 1.7 T with poor performance at higher temperature. In comparison, Hiperco50 is an iron cobalt vanadium soft magnetic alloy which exhibits high magnetic saturation (2.3 T) and low core loss [96]. This extra 0.6 T provided by Hiperco50 material would allow the motor size to be scaled down and the iron loss to be reduced. This will in turn increase the power density and efficiency of the motor. The Curie temperature of Hiperco50 is $940\,^{\circ}$C which can assure that it is able to work within the temperature range in the current design. Thus, we use Hiperco50 as the material for the stator and rotor. Besides, traditional wire insulation for the motor or generator applications is only capable of operating at the temperature limit of $200\,^{\circ}$C maximum. Thus, for other motor applications which will run in a higher temperature environment, we will need to use stainless steel clad copper wire with pre-ceramic polymer resins insulation, which can tolerate a temperature up to $700\,^{\circ}$C. However, due to the use of the ceramic material, the minimum bend radius of the wire is quite large, which may cause difficulty in assembly. Besides, in order to achieve the electrical connection of this type

of wire, welding rather than soldering must be chosen due to the stainless steel cladding.

We have designed a PM motor, which is able to run within a wide temperature range from -196 °C up to 300 °C. The designed motor is required to output 12 kW power at 12 krpm rotating speed with the efficiency greater than 90%. It is also required to work with good efficiency in a relatively wide speed range as well. We have developed our own tool to simulate the temperature variation of the residual flux density, copper loss, core loss, windage loss, etc. In the next section, we will introduce the key design methodology for this work. We will determine the most important dimensions of the design by our design tool, and we will further calculate and estimate its performance under various temperatures and speed conditions. Finally, we will provide results from the FEA analysis and confirm the initial design.

5.2 Design and Simulation Results

The design methodology for the PMSM with wide temperature range is basically similar with the one introduced in Chapter 2 with additional thoughts and considerations for the specific requirement on temperature. The key features of the designed motor are summarized in Table. 5.1, from which it can tell the volume of the motor, the net weight, the materials that will be used, and the key winding information, etc.

As discussed in Chapter 1 and Chapter 2, the electromagnet is basically made up of a stator tooth and the winding wrapped around it. The stator three-phase windings are excited by AC voltages converted through a DC to AC inverter. To avoid the magnetic saturation especially at the stator tooth area, we carefully design the dimensions of the slot as shown in Fig. 5.1. In addition, we purposely make the slot window area to be relatively large so that the "slot fill factor" is low due to the extra room is prepared for the insulation layers on such special design requirement of temperature. Based on the winding theory we discussed in chapter 2, we use double-layer lap winding for our design.

Table 5.1: Results of the PMSM design.

Machine Type	PMSM
Rated Output Power	12 kW
Rated Mechanical Speed	12 krpm
Rated Voltage	270 V
Number of Poles	6
Number of Stator Slots	24
Outer Diameter of Stator	165 mm
Inner Diameter of Stator	83.3 mm
Length of Machine	83.3 mm
Outer Diameter of Rotor	81.7 mm
Minimum Air Gap	0.8 mm
Type of Steel	Hiperco 50
Type of PM	SmCo 28
Max. Thickness of Magnet	1.4 mm
Number of Conductors per Slot	6
Copper Wire Diameter	4.62 mm
Stator Slot Fill Factor	52%
Total Machine Weight	13.4 kg
Efficiency	>90%

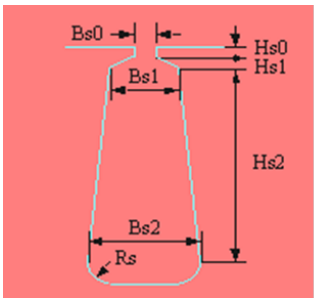

Figure 5.1: Dimensions of the stator slot.

According to the parameters in Table. 5.1, a complete structure of the PMSM is drawn in Fig. 5.2. The three-phase windings on the stator are marked in red, green and yellow, respectively.

It is emphasized that we make appropriate design of the shaft and housing to get enough room for the end-turns.

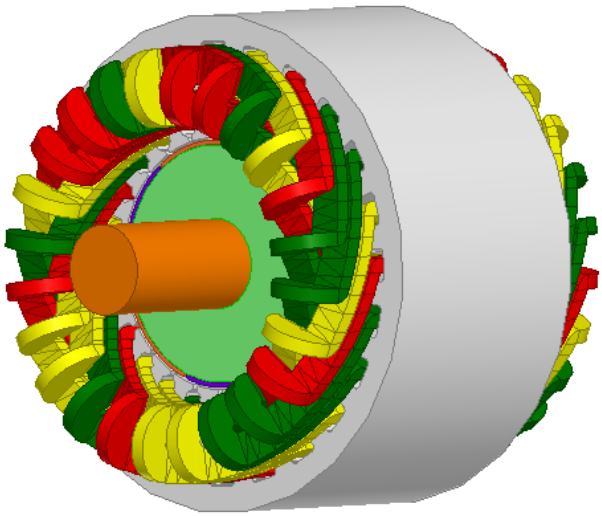

Figure 5.2: 24-slot 6-pole PMSM design.

The magnetic flux density (**B**) vector plot is shown in Fig. 5.3. It shows the vector distribution of the magnetic field while the motor is operating, from which we can verify that the magnetic path is correct [76].

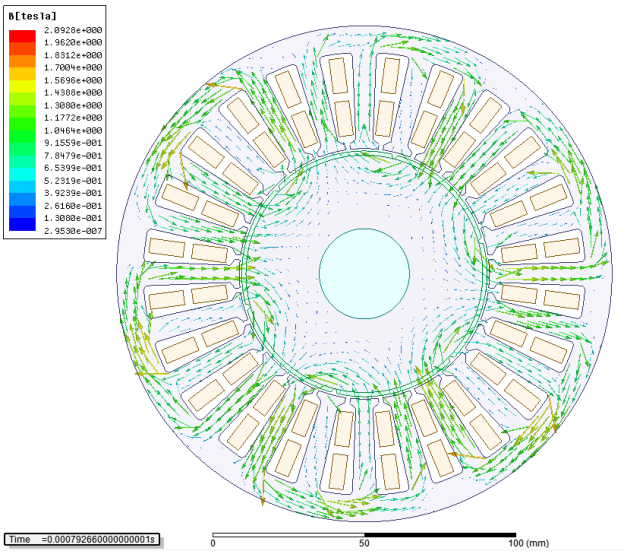

Figure 5.3: Flux density vector distribution.

We will show the plot of the magnitude distribution of the flux density (**B**) in 3D from Fig. 5.4 to Fig. 5.11, with the rotor rotates to a position of 45 degrees, 90 degrees, 135 degrees, 180 degrees, 225 degrees, 270 degrees, 325 degrees, 360 degrees, respectively. We can monitor the value of the peak flux density. The "rainbow" legend tells where the highest density is located at. We need to make the peak flux density under the control in order to avoid the magnetic saturation.

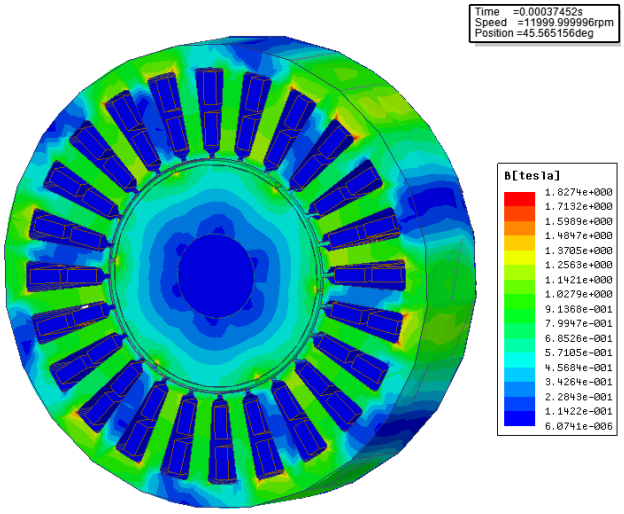

Figure 5.4: Magnitude distribution of the flux density (**B**) with rotor rotates 45 degrees.

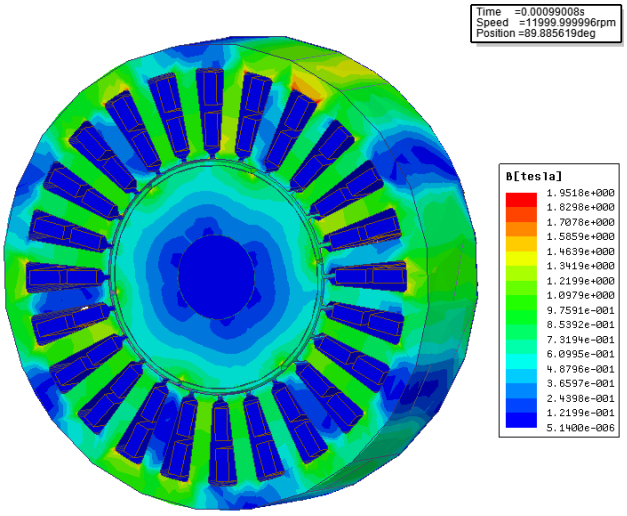

Figure 5.5: Magnitude distribution of the flux density (**B**) with rotor rotates 90 degrees.

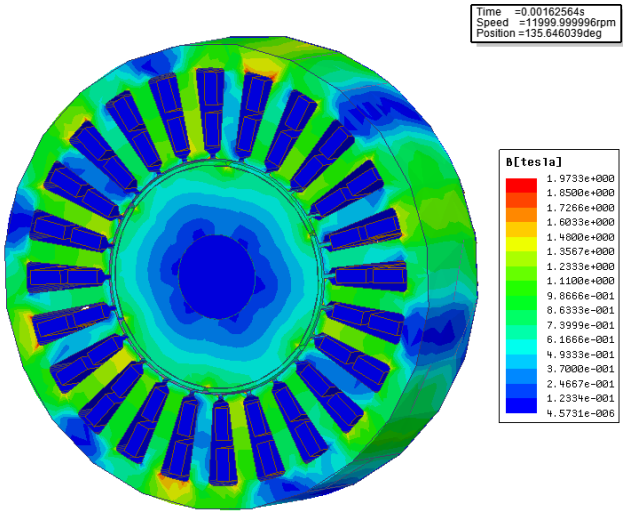

Figure 5.6: Magnitude distribution of the flux density (**B**) with rotor rotates 135 degrees.

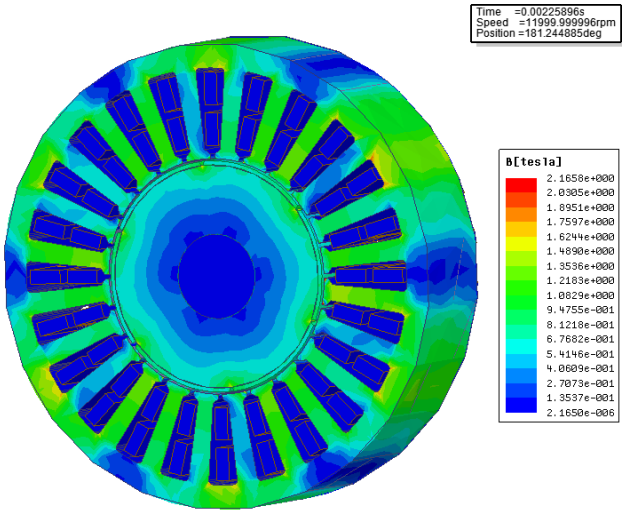

Figure 5.7: Magnitude distribution of the flux density (**B**) with rotor rotates 180 degrees.

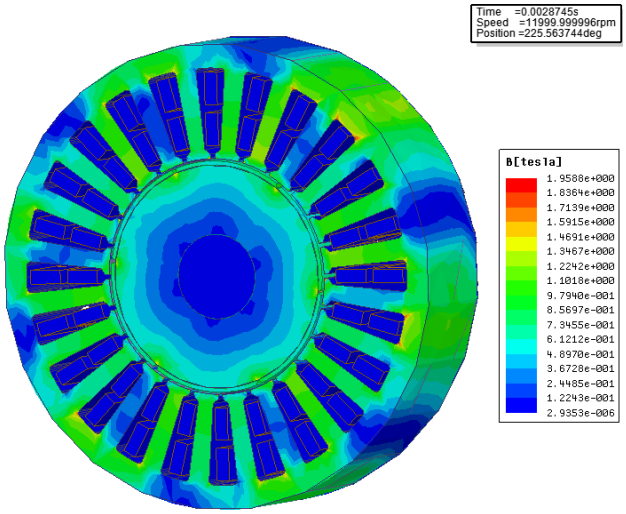

Figure 5.8: Magnitude distribution of the flux density (**B**) with rotor rotates 225 degrees.

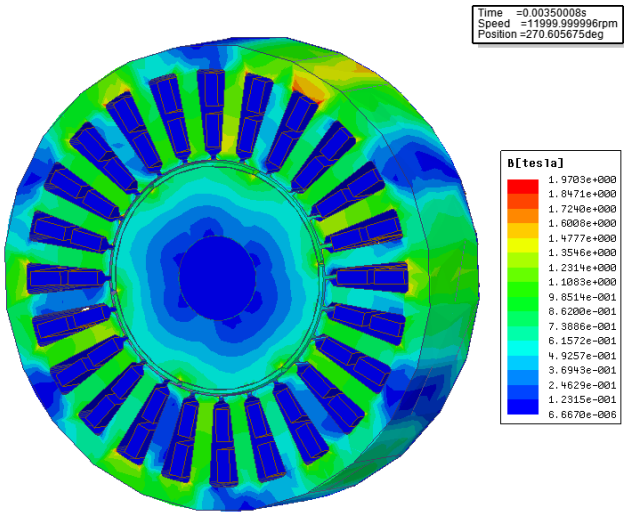

Figure 5.9: Magnitude distribution of the flux density (**B**) with rotor rotates 270 degrees.

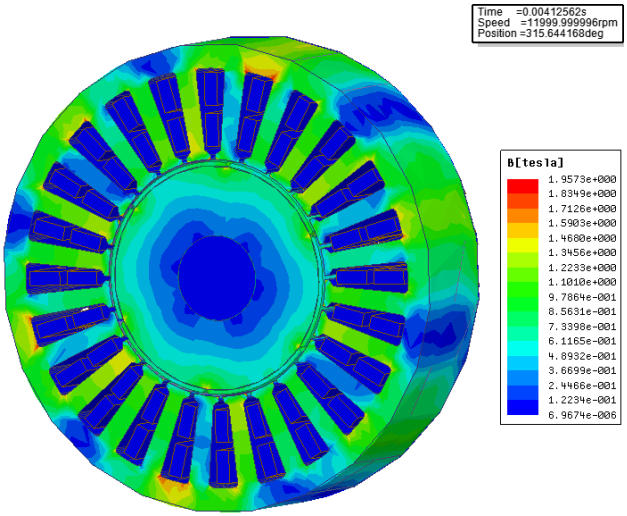

Figure 5.10: Magnitude distribution of the flux density (**B**) with rotor rotates 315 degrees.

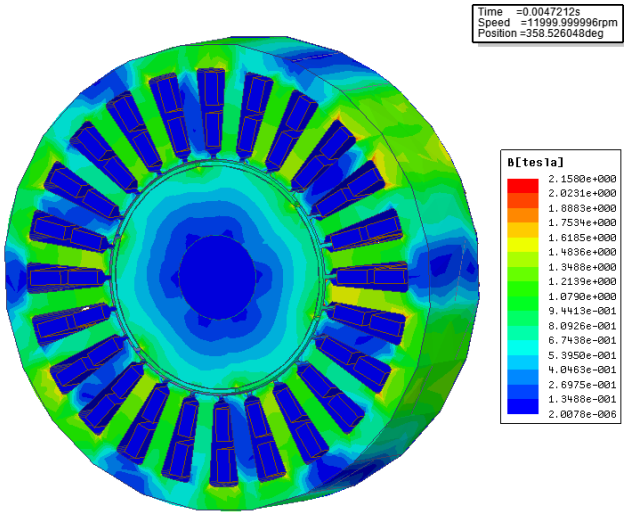

Figure 5.11: Magnitude distribution of the flux density (**B**) with rotor rotates 360 degrees.

The motor's winding currents from the simulation can be seen in Fig. 5.12. We will use this as a reference for the inverter design to ensure that the controller can hold that amount of phase current at full load.

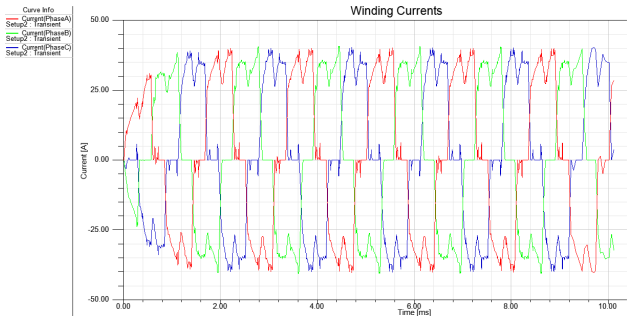

Figure 5.12: Winding currents.

The winding flux linkages are shown in Fig. 5.13. They are designed to be a sinusoidal distribution with harmonics and the simulation result proves that.

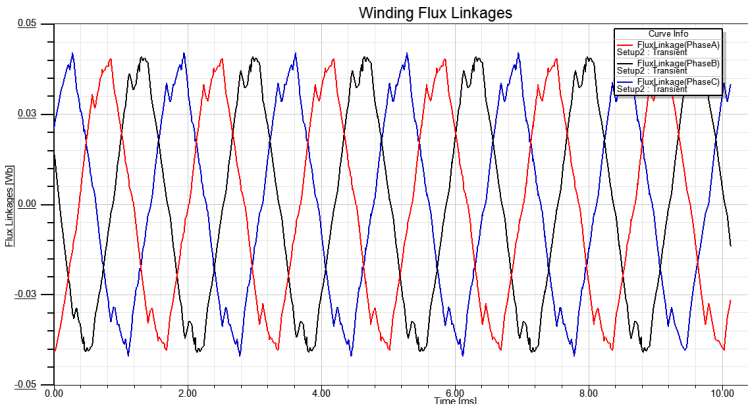

Figure 5.13: Winding flux linkages.

We consider all the effects discussed above to estimate the efficiency as a function of the rotating speed for various temperatures. With a wide temperature range from -196 °C up to 300 °C,

the efficiency is calculated by our analytic tool created in MATLAB, as shown in Fig. 5.14. It shows that the efficiency is inversely proportional to the temperature for certain speed range. However, with the speed further increasing up, the efficiency starts to be proportional to the temperature. The reason of that is because the windage loss decreases much faster due to the air property change than the copper loss increases when temperature increases.

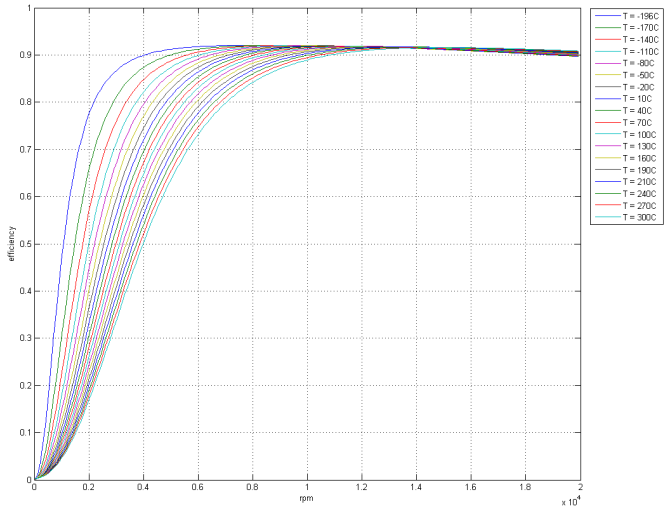

Figure 5.14: Efficiency as a function of the rotating speed for various temperatures.

5.3 Summary

We discussed the special thoughts and considerations for a PM motor design with wide temperature range from -196 °C up to 300 °C, including the analysis of the material property and performance. We have successfully developed and simulated the design with the efficiency greater than 90% at the designed speed of 12 krpm. The motor is able to run over a wide speed range, 8 krpm to 16 krpm. We have provided the design and simulation results. In addition, we have analyzed the performance of the motor according to the temperature influences based on numerical analysis, thereby helping to make this novel design a reality. With proper permanent magnet material, core material, and advanced pre-ceramic polymer resins insulation material, the motor can achieve its performance according to the design specifications. The future work of this design is to have the motor fabricated and the hardware tested.

CHAPTER 6: CONCLUSION

In this dissertation, we have developed a novel design methodology for a surface-mounted permanent magnet motor design. We have showed the key design procedure for a good start up design. Small torque angle is designed in order to increase the overload power handling capability and efficiency. Moreover, small torque angle results in a larger airgap and increased thickness of the permanent magnets, which helps to reduce the windage loss, noise and demagnetization. Therefore, new treatment of the MMF is developed through the integration due to the large size of the airgap. In order to boost up the efficiency of the PMSM, the most effective way is trying to reduce the copper loss. We use large cross section wire to reduce the resistance and thus reduce the copper loss. We use wide stator teeth structure to avoid the magnetic saturation, which results in less stator current and lower copper loss. Besides, we use large number of poles which decreases the required number of turns per coil, resulting in less slot areas and motor weight needed. We use stranded wire to reduce the AC copper loss. We have adjusted the size of the slot opening to reduce the cogging torque, which will result in a smooth electromagnetic torque.

We have implemented the design methodology into a 12-slot, 10-pole PMSM design as an energy conversion device for a truck all-electric battery-based APU system. We have also fabricated a prototype based on our design data. We have designed a three-phase sensorless inverter with the field oriented control scheme and sliding mode observer algorithm. We have tested the controller with the permanent magnet motor we designed and provided with the test results. In addition, we have researched on the thermal management of the PCB board and developed an inverter design with aluminum board structure targeting for higher power applications without the need for a cooling fan. It can significantly increase the power handling capability. Besides, we have researched on a novel design of a 24-slot, 6-pole PMSM that has the capability to work under an extreme temperature environment, which can be applied to some special applications. We proposed some considerations for the design and analyzed the performance of the motor according

to the temperature influences. The simulation results of the designed motor are also provided.

LIST OF REFERENCES

[1] Cros, J., Viarouge, P., and Halila, A., "Brush DC motors with concentrated windings and soft magnetic composites armatures," *Industry Applications Conference, 2001. Thirty-Sixth IAS Annual Meeting. Conference Record of the 2001 IEEE*, vol.4, no., pp.2549,2556, Sept. 30 2001-Oct. 4 2001.

[2] Ishak, D. and Abu Hassan, A.H., "Analytical modeling of permanent magnet excited brushed DC motor for low-cost applications," *Mechatronics and Its Applications, 2008. ISMA 2008. 5th International Symposium on*, vol., no., pp.1,5, 27-29 May. 2008.

[3] Carroll, James J., Schneider, M., and Dawson, D.M., "Integrator backstepping techniques for the tracking control of permanent magnet brush DC motors," *Industry Applications Society Annual Meeting, 1993., Conference Record of the 1993 IEEE*, vol.1, no., pp.663,671, 2-8 Oct. 1993.

[4] Asgari, S.H., Jannati, M., and Idris, N.R.N., "Modeling of three-phase induction motor with two stator phases open-circuit," *Energy Conversion (CENCON), 2014 IEEE Conference on*, vol., no., pp.231,236, 13-14 Oct. 2014.

[5] Carmona-Sanchez, J. and Ruiz-Vega, D., "Review of static induction motor models," *North American Power Symposium (NAPS), 2010*, vol., no., pp.1,8, 26-28 Sept. 2010.

[6] Cui, Shumei., Dai, Ying., and Song, Liwei., "Rotor Slots design of induction machine for hybrid electric vehicle drives," *Vehicle Power and Propulsion Conference, 2006. VPPC '06. IEEE*, vol., no., pp.1,3, 6-8 Sept. 2006.

[7] Mariut, L., Filip, M., Helerea, E., and Peter, I., "Analysis and modeling on the induction machine faults," *Electrical and Electronics Engineering (ISEEE), 2010 3rd International Symposium on*, vol., no., pp.11,16, 16-18 Sept. 2010.

[8] Tavares, A.M., Filho, A.F.F., and Blauth, Y.B., "A simple and low cost three-phase sector induction machine," *Electric Machines Drives Conference (IEMDC), 2011 IEEE International*, vol., no., pp.918,923, 15-18 May. 2011.

[9] Soter, S. and Wegener, R., "Development of induction machines in wind power technology," *Electric Machines & Drives Conference, 2007. IEMDC '07. IEEE International*, vol.2, no., pp.1490,1495, 3-5 May. 2007.

[10] Hecker, Q., Butron Ccoa, J.A., Meyer, W., and Herzog, H.-G., "Automated design of squirrel-cage induction machines by predefined torque-speed-characteristic," *Electric Machines Drives Conference (IEMDC), 2013 IEEE International*, vol., no., pp.1160,1165, 12-15 May. 2013.

[11] Petrushin, V., Petrushina, N.S., and Kalenik, B., "Designing of asynchronous induction machines for adjustable speed asynchronous electric drive systems," *Modern Problems of Radio Engineering, Telecommunications and Computer Science, 2008 Proceedings of International Conference on*, vol., no., pp.203,206, 19-23 Feb. 2008.

[12] Gonzalez, A., Hernandez, C., and Arjona, M.A., "A Novel High-Efficiency Parallel-Winding Connection for a Three-Phase Induction Motor Fed by a Single-Phase Power Supply," *Energy Conversion, IEEE Transactions on*, vol.29, no.2, pp.269,277, June. 2014.

[13] S. J. Chapman. "Electric Machinery Fundamentals," *McGraw-Hill, 4 Edition*, Oct 3, 2003.

[14] E.S. Hamdi. "Design of Small Electrical Machines," *John Wiley & Sons Ltd, 1 Edition*, Nov 1, 1994.

[15] R. Krishnan. "Switched Reluctance Motor Drives: Modeling, Simulation, Analysis, Design, and Applications (Industrial Electronics)," *CRC Press, 1 Edition*, June 28, 2001.

[16] T.J.E. Miller. "Electronic Control of Switched Reluctance Machines (Newnes Power Engineering Series)," *Newnes, 1 Edition*, July 9, 2001.

[17] Daohan Wang, Xiuhe Wang, and Chenghui Zhang, "Topology analysis and performance evaluation of a high thrust force density linear switched reluctance machine for low cost conveyor applications," *Electrical Machines and Systems (ICEMS), 2014 17th International Conference on*, vol., no., pp.1283,1288, 22-25 Oct. 2014.

[18] Byeong-Seok Lee, Han-Kyung Bae, Vijayraghavan, P., and Krishnan, R., "Design of a linear switched reluctance machine," *Industry Applications Conference, 1999. Thirty-Fourth IAS Annual Meeting. Conference Record of the 1999 IEEE*, vol.4, no., pp.2267,2274, 1999.

[19] Hao Chen and Gu, J.J., "Implementation of the three-phase switched reluctance machine system for motors and generators," *Mechatronics, IEEE/ASME Transactions on*, vol.15, no.3, pp.421,432, June. 2010.

[20] Arifin, A., Al-Bahadly, I., and Mukhopadhyay, S.C., "Analysis of a 12/16 switched reluctance machine using combined circuit and field computation," *Power Engineering and Optimization Conference (PEOCO), 2011 5th International*, vol., no., pp.170,175, 6-7 June. 2011.

[21] Jovanovic, M.G., Betz, R.E., and Jian Yu, "The use of doubly fed reluctance machines for large pumps and wind turbines," *Industry Applications, IEEE Transactions on*, vol.38, no.6, pp.1508,1516, Nov/Dec. 2002.

[22] I. Boldea. "Reluctance Synchronous Machines and Drives (Monographs in Electrical and Electronic Engineering)," *Oxford University Press, 1 Edition*, Aug 1, 1996.

[23] Ming Cheng, Chau, K.T., and Chan, C.C., "Design and analysis of a new salient permanent magnet motor," *Magnetics, IEEE Transactions on*, vol.37, no.4, pp. 3012,3020, Jul. 2001.

[24] Yuefeng Liao, Liang, F., and Lipo, T.A., "A novel permanent magnet motor with doubly salient structure," *Industry Applications Society Annual Meeting, 1992., Conference Record of the 1992 IEEE*, vol., no., pp.308,314, 4-9 Oct. 1992.

[25] D. C. Hanselman. "Brushless Permanent-Magnet Motor Design," *McGraw-Hill*, Jan 1, 1994.

[26] Sanada, M. and Morimoto, S., "Efficiency improvement in high speed operation using slotless configuration for permanent magnet synchronous motor," *Power Engineering Society General Meeting, 2007. IEEE*, vol., no., pp.1,7, 24-28 June. 2007.

[27] Sakai, K. and Yuzawa, N., "Realizing high efficiency using pole-changing hybrid permanent magnet motors," *Electric Machines Drives Conference (IEMDC), 2013 IEEE International*, vol., no., pp.462,467, 12-15 May. 2013.

[28] Jonq-Chin Hwang, Chuan-Sheng Liu, and Po-Cheng Chen, "Design of permanent-magnet synchronous gear motor with high efficiency for elevators," *Sustainable Energy Technologies (ICSET), 2012 IEEE Third International Conference on*, vol., no., pp.205,210, 24-27 Sept. 2012.

[29] Rix, A.J., Kamper, M.J., and Rong-Jie Wang, "Design and performance evaluation of concentrated coil permanent magnet machines for in-wheel drives," *Electric Machines Drives Conference, 2007. IEMDC '07. IEEE International*, vol.1, no., pp.770,775, 3-5 May. 2007.

[30] Liang Fang, Lee, B.H., Lee, J.J., Kim, H.J., and Jung-Pyo Hong, "Study on high-efficiency characteristics of interior permanent magnet synchronous motor with different magnet material," *Electrical Machines and Systems, 2009. ICEMS 2009. International Conference on*, vol., no., pp.1,4, 15-18 Nov. 2009.

[31] Krizan, J.A. and Sudhoff, S.D., "A Design model for salient permanent-magnet machines with investigation of saliency and wide-speed-range performance," *Energy Conversion, IEEE Transactions on*, vol.28, no.1, pp.95,105, March. 2013.

[32] Fengge Zhang, Jinhua Chen, and Guangwei Liu, "Research on counter-rotating dual rotors permanent-magnet machine for underwater vehicle," *Transportation Electrification Asia-Pacific (ITEC Asia-Pacific), 2014 IEEE Conference and Expo*, vol., no., pp.1,7, Aug. 31-Sept. 3 2014.

[33] Wei Wang, Chenjie Lin, and Fahimi, B., "Comparative analysis of double stator switched reluctance machine and permanent magnet synchronous machine," *Industrial Electronics (ISIE), 2012 IEEE International Symposium on*, vol., no., pp.617,622, 28-31 May. 2012.

[34] Wang, K., Zhu, Z.Q., Ombach, G., Koch, M., Zhang, S., and Xu, J., "Electromagnetic performance of an 18-Slot/10-Pole fractional-slot surface-mounted permanent-magnet machine," *Industry Applications, IEEE Transactions on*, vol.50, no.6, pp.3685,3696, Nov.-Dec. 2014.

[35] Yue Ma, Wei Zhang, Yi Yang, and Bao, H., "Research on loss of axial field flux-switching permanent magnet machine," *Electrical Machines and Systems (ICEMS), 2014 17th International Conference on*, vol., no., pp.1145,1149, 22-25 Oct. 2014.

[36] Akita, H., Nakahara, Y., Miyake, N., and Oikawa, T., "New core structure and manufacturing method for high efficiency of permanent magnet motors," *Industry Applications Conference, 2003. 38th IAS Annual Meeting. Conference Record of the*, vol.1, no., pp.367,372, 12-16 Oct. 2003.

[37] Nobels, T., Gheysen, T., Vanhove, M., and Stevens, S., "Design considerations for a plug-in hybrid car electrical motor," *Clean Electrical Power, 2009 International Conference on*, vol., no., pp.755,759, 9-11 June. 2009.

[38] Lin Bai, "Electric drive system with BLDC motor," *Electric Information and Control Engineering (ICEICE), 2011 International Conference on*, vol., no., pp.359,363, 15-17 April. 2011.

[39] Bouhoune, K., Yazid, K., and Boucherit, M.S., "Hybrid control of the two-phase induction machine," *Electrical Machines (ICEM), 2012 XXth International Conference on*, vol., no., pp.973,979, 2-5 Sept. 2012.

[40] Jinsong Kang, Guoqing Xu, Bo Hu, Zhouyun Zhang, and Jun Gong, "Research on field-weakening based on reactive power with BLDC motor for electric vehicle application," *Inte-*

gration Technology, 2007. ICIT '07. IEEE International Conference on, vol., no., pp.437,441, 20-24 March. 2007.

[41] Rahim, N.A., Hew Wooi Ping, and Tadjuddin, M., "Design of axial flux permanent magnet brushless DC motor for direct drive of electric vehicle," *Power Engineering Society General Meeting, 2007. IEEE*, vol., no., pp.1,6, 24-28 June. 2007.

[42] Chen, G.H. and Tseng, K.J., "Design of a permanent-magnet direct driven wheel motor drive for electric vehicle," *Power Electronics Specialists Conference, 1996. PESC '96 Record., 27th Annual IEEE*, vol.2, no., pp.1933,1939, 23-27 Jun. 1996.

[43] Yee-Pien Yang and Down Su Chuang, "Optimal design and control of a wheel motor for electric passenger cars," *Magnetics, IEEE Transactions on*, vol.43, no.1, pp.51,61, Jan. 2007.

[44] Qianfan Zhang and Xiaofei Liu, "Permanent magnetic synchronous motor and drives applied on a mid-size hybrid electric car," *Vehicle Power and Propulsion Conference, 2008. VPPC '08. IEEE*, vol., no., pp.1,5, 3-5 Sept. 2008.

[45] Zheng Ping, Liu Yong, Wang Yan, and Cheng Shukang, "Magnetization analysis of the brushless DC motor used for hybrid electric vehicle," *Electromagnetic Launch Technology, 2004. 2004 12th Symposium on*, vol., no., pp.542,545, 25-28 May. 2005.

[46] Nerg, J., Rilla, M., Ruuskanen, V., Pyrhonen, J., and Ruotsalainen, S., "Design of direct-driven permanent magnet synchronous motors for an electric sports car," *Electrical Machines (ICEM), 2012 XXth International Conference on*, vol., no., pp.177,182, 2-5 Sept. 2012.

[47] Williamson, S.S., Lukic, S.M., and Emadi, A., "Comprehensive drive train efficiency analysis of hybrid electric and fuel cell vehicles based on motor-controller efficiency modeling," *Power Electronics, IEEE Transactions on*, vol.21, no.3, pp.730,740, May. 2006.

[48] Zaiyun Zong, Li Quan, and Zixuan Xiang, "Comparison of double-stator flux-switching permanent magnet machine and double-stator permanent magnet synchronous machine for

electric vehicle applications," *Electrical Machines and Systems (ICEMS), 2014 17th International Conference on*, vol., no., pp.234,239, 22-25 Oct. 2014.

[49] Chin, Y.K. and Soulard, J., "A permanent magnet synchronous motor for traction applications of electric vehicles," *Electric Machines and Drives Conference, 2003. IEMDC'03. IEEE International*, vol.2, no., pp.1035,1041, 1-4 June. 2003.

[50] Dilmi, S. and Yurkovich, S., "Nonlinear torque control of the induction motor in hybrid electric vehicle applications," *American Control Conference, 2005. Proceedings of the 2005*, vol.5, no., pp.3001,3006, 8-10 June. 2005.

[51] Jiabin Wang, Xibo Yuan, and Atallah, K., "Design optimization of a surface-mounted permanent-magnet motor with concentrated windings for electric vehicle applications," *Vehicular Technology, IEEE Transactions on*, vol.62, no.3, pp.1053,1064, March. 2013.

[52] Habib Ullah, M., Gunawan, T.S., Sharif, M.R., and Muhida, R., "Design of environmental friendly hybrid electric vehicle," *Computer and Communication Engineering (ICCCE), 2012 International Conference on*, vol., no., pp.544,548, 3-5 July. 2012.

[53] Bertoni, L., Gualous, H., Bouquain, D., Hissel, D., Pera, M.-C., and Kauffmann, J.-M., "Hybrid auxiliary power unit (APU) for automotive applications," *Vehicular Technology Conference, 2002. Proceedings. VTC 2002-Fall. 2002 IEEE 56th*, vol.3, no., pp.1840,1845, 2002.

[54] Xiaogang Wu, Fuyuan Yang, Languang Lu, and Minggao Ouyang, "Dynamic control for low cost auxiliary power unit of electric bus," *Electronic and Mechanical Engineering and Information Technology (EMEIT), 2011 International Conference on*, vol.2, no., pp.1045,1049, 12-14 Aug. 2011.

[55] Gualous, H., Hissel, D., Bontour, S., Harel, F., and Kauffmann, J.-M., "Power management of an embedded fuel cell-supercapacitor APU," *Power Electronics and Applications, 2005 European Conference on*, vol., no., pp.8 pp.,P.8.

[56] Li Yu, Zhuoran Zhang, Zhihui Chen, and Yangguang Yan, "Analysis and verification of the doubly salient brushless DC generator for automobile auxiliary power unit application," *Industrial Electronics, IEEE Transactions on*, vol.61, no.12, pp.6655,6663, Dec. 2014.

[57] Bin He and Minggao Yang, "Robust LPV control of diesel auxiliary power unit for series hybrid electric vehicles," *Power Electronics, IEEE Transactions on*, vol.21, no.3, pp.791,798, May. 2006.

[58] Naidu, M., Nehl, T.W., Gopalakrishnan, S., and Wurth, L., "A semi-integrated sensorless PM brushless drive for a 42 V automotive HVAC compressor," *Industry Applications Conference, 2003. 38th IAS Annual Meeting. Conference Record of the*, vol.3, no., pp.1435,1442, 12-16 Oct. 2003.

[59] Hong Zhang, Zhaoyang He, and Yunlong Wang, "Control strategy research of auxiliary power unit in range-extended electric bus," *Transportation Electrification Asia-Pacific (ITEC Asia-Pacific), 2014 IEEE Conference and Expo*, vol., no., pp.1,4, Aug. 31-Sept. 3 2014.

[60] Kabisch, M., Heuer, M., Heideck, G., and Styczynski, Z.A., "Energy management of vehicle electrical system with auxiliary power unit," *Vehicle Power and Propulsion Conference, 2009. VPPC '09. IEEE*, vol., no., pp.358,363, 7-10 Sept. 2009.

[61] Dalal, A. and Smith, J., "Design and development of a plug-in auxiliary power unit for heavy duty vehicle applications and stationary vocational equipment," *Vehicle Power and Propulsion Conference (VPPC), 2011 IEEE*, vol., no., pp.1,5, 6-9 Sept. 2011.

[62] Yabsley, A. and Ibrahim, Y., "Study on maintenance contribution to Life Cycle Costs: Aircraft Auxiliary Power Unit example," *Industrial Technology, 2008. ICIT 2008. IEEE International Conference on*, vol., no., pp.1,6, 21-24 April. 2008.

[63] Fiengo, G., Glielmo, L., and Vasca, Francesco., "Control of Auxiliary Power Unit for hybrid electric vehicles," *Control Systems Technology, IEEE Transactions on*, vol.15, no.6, pp.1122,1130, Nov. 2007.

[64] Liu, H. et al., "High Efficiency Permanent Magnet Machine," *US Patent 8829742*, July. 2014.

[65] Surong Huang, Jian Luo, Leonardi, F., and Lipo, T.A., "A general approach to sizing and power density equations for comparison of electrical machines," *Industry Applications Conference, 1996. Thirty-First IAS Annual Meeting, IAS '96., Conference Record of the 1996 IEEE*, vol.2, no., pp.836,842, 6-10 Oct. 1996.

[66] Honsinger, V.B., "Sizing equations for electrical machinery," *Power Engineering Review, IEEE*, vol.PER-7, no.3, pp.39,40, March. 1987.

[67] Liu, H. et al., "Design and optimization of permanent magnet switch reluctance machine for renewable energy application," *Electrical Machines (ICEM), 2012 XXth International Conference on*, vol., no., pp.612-617, 2-5 Sept. 2012.

[68] H.C.J.de Jong. "AC Motor Design: Rotating Magnetic Fields in a Changing Environment," *Hemisphere Publishing Corporation*, 1989.

[69] Zheng, L., Wu, T.X., Acharya, D., Sundaram, K.B., Vaidya, J., Zhao, L., Ham, C.H., Arakere, N., Kapat, J., and Chow, L., "Super-high speed cryogenic PMSM design," *Magnetics Conference, 2005. INTERMAG Asia 2005. Digests of the IEEE International*, vol., no., pp.1961,1962, 4-8 April. 2005.

[70] Cavagnino, A., Lazzari, M., Profumo, F., and Tenconi, A., "A comparison between the axial flux and the radial flux structures for PM synchronous motors," *Industry Applications, IEEE Transactions on*, vol.38, no.6, pp.1517,1524, Nov/Dec. 2002.

[71] Profumo, F., Tenconi, A., Zhang, Z., and Cavagnino, A., "Novel axial flux interior PM synchronous motor realized with powdered soft magnetic materials," *Industry Applications Conference, 1998. Thirty-Third IAS Annual Meeting. The 1998 IEEE*, vol.1, no., pp.152,158, 12-15 Oct. 1998.

[72] Zhu, Z.Q. and Howe, D., "Magnetic field analysis and inductances of brushless DC machines with surface-mounted magnets and non-overlapping stator windings," *Magnetics, IEEE Transactions on*, vol.31, no.3, pp.2115,2118, May. 1995.

[73] Bianchi, N. and Bolognani, S., "Design techniques for reducing the cogging torque in surface-mounted PM motors," *Industry Applications, IEEE Transactions on*, vol.38, no.5, pp.1259,1265, Sep/Oct. 2002.

[74] Liuchen Chang, "An improved FE inductance calculation for electrical machines," *IMagnetics, IEEE Transactions on*, vol.32, no.4, pp.3237,3245, July. 1996.

[75] Levi, E., "Saturation modelling in d-q axis models of salient pole synchronous machines," *Energy Conversion, IEEE Transactions on*, vol.14, no.1, pp.44,50, Mar. 1999.

[76] Liu, H. et al., "Design of high speed universal motor for organic agriculture applications," *Progress in Electromagnetics Research Symposium (PIERS), Session 1P6: 197*, 5-8 July. 2010.

[77] Dorrell, D.G., Hsieh, M., Popescu, M., Evans, L., Staton, D.A., and Grout, V., "A review of the design issues and techniques for radial-flux brushless surface and internal rare-earth permanent-magnet motors," *IEEE Transactions on Industrial Electronics*, vol.58, no.9, pp.3741,3757, Sept. 2011.

[78] S. J. Salon. "Finite Element Analysis of Electrical Machines," *Kluwer Academic Publishers*, 1995.

[79] Shimoji, H., Enokizono, M., and Todaka, T., "Iron loss and magnetic fields analysis of permanent magnet motors by improved finite element method with E& S model," *Magnetics, IEEE Transactions on*, vol.37, no.5, pp.3526,3529, Sept. 2001.

[80] J. P. A. Bastos and N. Sadowski. "Electromagnetic Modeling by Finite Element Methods, *CRC Press*, April 1, 2003.

[81] Chari, M.V.K., "Finite element analysis of electrical machinery and devices," *Magnetics, IEEE Transactions on*, vol.16, no.5, pp.1014,1019, Sept. 1980.

[82] Pavlik, D., Garg, V.K., Repp, J.R., and Weiss, J., "A finite element technique for calculating the magnet sizes and inductances of permanent magnet machines," *Energy Conversion, IEEE Transactions on*, vol.3, no.1, pp.116,122, Mar. 1988.

[83] Guo, Y.G. and Zhu, J.G., "Improved methods for force and torque calculation in electrical machines by 3D finite element analysis," *Electrical Machines and Systems, 2001. ICEMS 2001. Proceedings of the Fifth International Conference on*, vol.2, no., pp.1191,1194, Aug. 2001.

[84] Fouad, F.A., Nehl, T.W., and Demerdash, N.A., "Magnetic field modeling of permanent magnet type electronically operated synchronous machines using finite elements," *Power Apparatus and Systems, IEEE Transactions on*, vol.PAS-100, no.9, pp.4125,4135, Sept. 1981.

[85] Miller, T.J.E., Popescu, M., Cossar, C., McGilp, M.I., Olaru, M., Davies, A., Sturgess, J., and Sitzia, A., "Embedded finite-element solver for computation of brushless permanent-magnet motors," *Industry Applications, IEEE Transactions on*, vol.44, no.4, pp.1124,1133, July.-Aug. 2008.

[86] Ionel, D.M., Popescu, M., McGilp, M., Miller, T.J.E., and Dellinger, S., "Assessment of torque components in brushless permanent magnet machines through numerical analysis of the electromagnetic field," *Industry Applications Conference, 2004. 39th IAS Annual Meeting. Conference Record of the 2004 IEEE*, vol.3, no., pp.1715,1722, 3-7 Oct. 2004.

[87] Gieras, J.F., Santini, E., and Wing, M., "Calculation of synchronous reactances of small permanent-magnet alternating-current motors: comparison of analytical approach and finite element method with measurements," *Magnetics, IEEE Transactions on*, vol.34, no.5, pp.3712,3720, Sep. 1998.

[88] Demerdash, N.A. and Nehl, T.W., "Electric machinery parameters and torques by current and energy perturbations from field computations.I:theory and formulation and II: applications and results," *Electric Machines and Drives Conference Record, 1997. IEEE International*, vol., no., pp.TA1/1.1,TA1/1.6, 18-21 May. 1997.

[89] G. Meunier. "The Finite Element Method for Electromagnetic Modeling," *Wiley-ISTE, 1 Edition*, Nov, 2008.

[90] Trlep, M., Skerget, L., Kreca, B., and Hribernik, B., "Hybrid finite-element-boundary element method for nonlinear electromagnetic problems," *Magnetics, IEEE Transactions on*, vol.31, no.3, pp.1380,1383, May. 1995.

[91] G. H. W. Beaty and J. L. Kirtley. Jr. "Electric Motor Handbook," *McGraw-Hill*, 1998.

[92] J.F. Gieras. "Advancements in Electric Machines," *Springer*, 2008.

[93] Binesti, D. and Ducreux, J.P., "Core losses and efficiency of electrical motors using new magnetic materials," *Magnetics, IEEE Transactions on*, vol.32, no.5, pp.4887,4889, Sept. 1996.

[94] Siemon, G.R. and Liu, X., "Core losses in permanent magnet motors," *Magnetics, IEEE Transactions on*, vol.26, no.5, pp.1653,1655, Sept. 1990.

[95] Zhou, P., Lin, D., Xiao, Y., Lambert, N., and Rahman, M.A., "Temperature-dependent demagnetization model of permanent magnets for finite element analysis," *Magnetics, IEEE Transactions on*, vol.48, no.2, pp.1031,1034, Feb. 2012.

[96] Liu, H. et al., "Design of a permanent magnet motor with wide temperature range," *12th Joint MMM-Intermag Conference*, vol., no., 14-18, Jan. 2013.

[97] Rosu, M., Arkkio, A., Jokinen, T., Mantere, J., and Westerlund, J., "Demagnetization state of permanent magnets in large output power permanent magnet synchronous motor," *Electric*

Machines and Drives, 1999. International Conference IEMD '99, vol., no.,pp.776,778, May. 1999.

[98] J.R. Hendershot and T.J.E Miller. "Design of Brushless permanent-Magnet Machines," *Motor Design Books LLC, 2 Edition*, 20 Mar, 2010.

[99] Miller, T.J.E., McGilp, M.I., Staton, D.A., and Bremner, J.J., "Calculation of inductance in permanent-magnet DC motors," *Electric Power Applications, IEE Proceedings*, vol.146, no.2, pp.129,137, March. 1999.

[100] Reddy, P.B., EL-Refaie, A.M., Kum-Kang Huh, Tangudu, J.K., and Jahns, T.M., "Comparison of interior and surface PM machines equipped with fractional-slot concentrated windings for hybrid traction applications," *Energy Conversion, IEEE Transactions on*, vol.27, no.3, pp.593,602, Sept. 2012.

[101] Cros, J. and Viarouge, P., "Synthesis of high performance PM motors with concentrated windings," *Electric Machines and Drives, 1999. International Conference IEMD '99*, vol., no., pp.725,727, May. 1999.

[102] Magnussen, F. and Sadarangani, C., "Winding factors and Joule losses of permanent magnet machines with concentrated windings," *Electric Machines and Drives Conference, 2003. IEMDC'03. IEEE International*, vol.1, no., pp.333,339, 1-4 June. 2003.

[103] Evans, D., Azar, Z., Wu, L.J., and Zhu, Z.Q., "Comparison of optimal design and performance of PM machines having non-overlapping windings and different rotor topologies," *Power Electronics, Machines and Drives (PEMD 2010), 5th IET International Conference on*, vol., no., pp.1,7, 19-21 April. 2010.

[104] Shima, K., Ide, K., Takahashi, M., Yoshinari, Y., and Nitobe, M., "Calculation of leakage inductances of a salient-pole synchronous machine using finite elements," *Energy Conversion, IEEE Transactions on*, vol.14, no.4, pp.1156,1161, Dec. 1999.

[105] Bon-Ho Bae, Seung-Ki Sul, Jeong-Hyeck Kwon, and Jong-Sub Shin, "Implementation of sensorless vector control for super-high speed PMSM of turbo-compressor," *Industry Applications Conference, 2001. Thirty-Sixth IAS Annual Meeting. Conference Record of the 2001 IEEE*, vol.2, no., pp.1203,1209, Sept. 30-Oct. 4 2001.

[106] Schaible, U. and Szabados, B., "Dynamic motor parameter identification for high speed flux weakening operation of brushless permanent magnet synchronous machines," *Energy Conversion, IEEE Transactions on*, vol.14, no.3, pp.486,492, Sept. 1999.

[107] Chee-Mun Ong. "Dynamic Simulation of Electric Machinery," *Prentice-Hall*, 1998.

[108] Senjyu, T., Kuwae, Y., Urasaki, N., and Uezato, K., "Accurate parameter measurement for high speed permanent magnet synchronous motors," *Power Electronics Specialists Conference, 2001. PESC. 2001 IEEE 32nd Annual*, vol.2, no., pp.772,777, 2001.

[109] Stumberger, B., Kreca, B., and Hribernik, B., "Determination of parameters of synchronous motor with permanent magnets from measurement of load conditions," *Energy Conversion, IEEE Transactions on*, vol.14, no.4, pp.1413,1416, Dec. 1999.

[110] Gorman, S.F., Chen, C., and Cathey, J.J., "Determination of permanent magnet synchronous motor parameters for use in brushless DC motor drive analysis," *Energy Conversion, IEEE Transactions on*, vol.3, no.3, pp.674,681, Sept. 1988.

[111] Longya Xu and Changjiang Wang, "Implementation and experimental investigation of sensorless control schemes for PMSM in super-high variable speed operation," *Industry Applications Conference, 1998. Thirty-Third IAS Annual Meeting. The 1998 IEEE*, vol.1, no., pp.483,489, 12-15 Oct. 1998.

[112] Masaki, R., Kaneko, S., Hombu, M., Sawada, T., and Yoshihara, S., "Development of a position sensorless control system on an electric vehicle driven by a permanent magnet synchronous motor," *Power Conversion Conference, 2002. PCC-Osaka 2002. Proceedings of the*, vol.2, no., pp.571,576, 2002.

[113] Leksell, M., Harnefors, L., and Jansson, M., "Direct sensorless speed control of PM-motors a simple and effective sensorless method," *Power Electronics Specialists Conference, 2001. PESC. 2001 IEEE 32nd Annual*, vol.2, no., pp.805,810, 2001.

[114] Mobarakeh, B.N., Meibody-Tabar, F., and Sargos, F.M., "Robustness study of a model-based technique for mechanical sensorless PMSM," *Power Electronics Specialists Conference, 2001. PESC. 2001 IEEE 32nd Annual*, vol.2, no., pp.811,816, 2001.

[115] Guchuan Zhu, Kaddouri, A., Dessaint, L.-A., and Akhrif, O., "A nonlinear state observer for the sensorless control of a permanent-magnet AC machine," *Industrial Electronics, IEEE Transactions on*, vol.48, no.6, pp.1098,1108, Dec. 2001.

[116] Tursini, M., Chiricozzi, E., and Petrella, R., "Flux-weakening control of surface mounted PM synchronous motors accounting for resistive voltage drop," *Electrical Machines, 2008. ICEM 2008. 18th International Conference on*, vol., no., pp.1,6, 6-9 Sept. 2008.

[117] Consoli, A., Scarcella, G., and Testa, A., "Industry application of zero-speed sensorless control techniques for PM synchronous motors," *Industry Applications, IEEE Transactions on*, vol.37, no.2, pp.513,521, March/April. 2001.

[118] Ji-Hoon Jang, Seung-Ki Sul, Jung-Ik Ha, Ide, K., and Sawamura, M., "Sensorless drive of SMPM motor by high frequency signal injection," *Applied Power Electronics Conference and Exposition, 2002. APEC 2002. Seventeenth Annual IEEE*, vol.1, no., pp.279,285, 2002.

[119] A. E. Fitzgerald, C. Kingsley Jr, and S.D. Umans. "Electric Machinery," *McGraw-Hill Science/Engineering/Math, 7 Edition*, Jan 28, 2013.

[120] P.C. Krause, O. Wasynczuk, and S.D. Sudhoff. "Analysis of Electric Machinery and Drive Systems," *Wiley-IEEE Press, 2 Edition*, Mar 5, 2002.

[121] Bin Wu. "High-Power Converters and AC Drives," *Wiley-IEEE Press, 1 Edition*, Mar 17, 2006.

[122] R. Krishnan. "Permanent Magnet Synchronous and Brushless DC Motor Drives," *CRC Press*, Sep 25, 2009.

[123] Hui, T.S., Basu, K.P., and Subbiah, V., "Permanent magnet brushless motor control techniques," *Power Engineering Conference, 2003. PECon 2003. Proceedings. National*, vol., no., pp.133,138, 15-16 Dec. 2003.

[124] Verghese, George C., Lang, Jeffrey H., and Casey, L.F., "Analysis of instability in electrical machines," *Industry Applications, IEEE Transactions on*, vol.IA-22, no.5, pp.853,864, Sept. 1986.

[125] Perera, P.D.C., Blaabjerg, F., Pedersen, J.K., and Thogersen, P., "A sensorless, stable V/f control method for permanent-magnet synchronous motor drives," *Industry Applications, IEEE Transactions on*, vol.39, no.3, pp.783,791, May.-June. 2003.

[126] Parasiliti, F., Petrella, R., and Tursini, M., "Sensorless speed control of a PM synchronous motor by sliding mode observer," *Industrial Electronics, 1997. ISIE '97., Proceedings of the IEEE International Symposium on*, vol.3, no., pp.1106,1111, 7-11 Jul. 1997.

[127] Colby, R.S. and Novotny, D.W., "An efficiency-optimizing permanent-magnet synchronous motor drive," *Industry Applications, IEEE Transactions on*, vol.24, no.3, pp.462,469, May/Jun. 1988.

[128] Jahns, T.M., "Motion control with permanent-magnet AC machines," *Proceedings of the IEEE*, vol.82, no.8, pp.1241,1252, Aug. 1994.

[129] Itoh, J.-I., Nomura, N., and Ohsawa, Hiroshi, "A comparison between V/f control and position-sensorless vector control for the permanent magnet synchronous motor," *Power Conversion Conference, 2002. PCC-Osaka 2002. Proceedings of the*, vol.3, no., pp.1310,1315, 2002.

[130] C. Smith and J. Peters. "Thermal Analysis of a PCB Assembly," *Phoenix Analysis & Design Technologies*, Dec 7, 2011.

[131] J. Zhang. "Choosing the right power MOSFET package," *International Rectifier*, Feb, 2004.

[132] Bulut, Y. and Pandya, K., "Thermal modeling for power MOSFETs in DC/DC applications," *Thermal and Mechanical Simulation and Experiments in Microelectronics and Microsystems, 2004. EuroSimE 2004. Proceedings of the 5th International Conference on*, vol., no., pp.429,433, 2004.

[133] Plotog, I., Varzaru, G., Bunea, R., Busu, I., Cucu, T., and Svasta, P., "Investigation on the efficiency of thermal relief shapes on different Printed Circuit Boards," *Design and Technology in Electronic Packaging (SIITME), 2010 IEEE 16th International Symposium for*, vol., no., pp.287,290, 23-26 Sept. 2010.

[134] Po-Wen Hwang, Hsien-Chie Cheng, Jiunn Fang, and Jia-Han Li, "CFD-based thermal characterization of board-level microelectronic devices under natural convection cooling," *Microsystems, Packaging, Assembly and Circuits Technology, 2007. IMPACT 2007. International*, vol., no., pp.79,82, 1-3 Oct. 2007.

[135] Lohan, J., Tiilikka, P., Fager, C.-M., and Rantala, J., "Effect of both PCB thermal conductivity and nature of forced convection environment on component operating temperature: Experimental measurement and numerical prediction," *Semiconductor Thermal Measurement and Management Symposium, 2000. Sixteenth Annual IEEE*, vol., no., pp.128,139, 2000.

[136] Lee, G. and Lin, J., "The introduction of high heat dissipation material," *Microsystems, Packaging, Assembly and Circuits Technology Conference, 2009. IMPACT 2009. 4th International*, vol., no., pp.240,243, 21-23 Oct. 2009.

[137] Pandya, K., "Thermal analysis of power MOSFETs using Rebeca-3D thermal modeling software (from Epsilon Ingenierie) versus physical measurements and possible extractions," *Thermal, Mechanical and Multi-Physics Simulation and Experiments in Micro-Electronics and Micro-Systems, 2005. EuroSimE 2005. Proceedings of the 6th International Conference on*, vol., no., pp.394,397, 18-20 April. 2005.